Modulation of Polar Mesospheric Summer Echoes (PMSE) ~~during~~ with HF Heating during low solar illumination

Tinna L. Gunnarsdottir [1], Arne Poggenpohl [1,2], Ingrid Mann [1], Alireza Mahmoudian [3], Peter Dalin [4], Ingemar Haeggstroem [5], and Michael Rietveld [6]

[1]Department of Physics and Technology, UiT Arctic University of Norway, Tromsø, Norway
[2]Physics Faculty, TU Dortmund University, Germany
[3]Institude of Geophysics, University of Tehran, Iran
[4]Swedish Institute of Space Physics, IRF, Kiruna, Sweden
[5]EISCAT Scientific Association, Kiruna, Sweden
[6]EISCAT Scientific Association, Ramfjord, Norway

Correspondence: Tinna Gunnarsdottir (tinna.gunnarsdottir@uit.no)

Abstract.

~~The formation of~~ Polar Mesospheric Summer Echoes (PMSE) formation is linked to ~~the presence of~~ charged dust/ice particles in the mesosphere~~and the PMSE modulation is a possible way to observe the effect of dust charging.~~ . We investigate the modulation of PMSE ~~by HF radio waves~~ with radiowaves based on measurements ~~carried out with the EISCAT Heating facility and the EISCAT VHF radar in August 2018 and August 2020 toward the end of the PMSE season~~ with EISCAT VHF radar and EISCAT Heating Facility during low solar illumination. The measurements were made ~~during the night with reduced solar illumination. The EISCAT~~ in August 2018 and 2020 around 20-02 UT. Heating was operated in ~~subsequent~~ cycles of 48 s on and 168 s off intervals. ~~In our observations, the PMSE modulation by the HF heating disappears during ionospheric conditions of energetic particle precipitation. We observe more~~ More than half of the ~~cycles being influenced by the heating with a reduced PMSE power~~ observed heating cycles show a PMSE modulation with a decrease in PMSE when the heater is on and ~~a similar amount of cycles showing an increase in power when the heater is turned off . In less~~ an increase when it is switched off again. The PMSE often increases beyond its initial strength. Less than half of the observed ~~cycles we see an overshoot~~ ~~and it seems to be largely influenced by the overall PMSE power; with smaller or nonexistent overshoot when the PMSE power is high~~ modulations have such an overshoot. The overshoots are small or nonexistent at strong PMSE; neither are they observed when the ionosphere is influenced by particle precipitation. We observe instances of very large overshoots ~~, where background PMSE~~ ~~power seems to be reduced. During periods when we observe modulation , they often vary~~ at weak PMSE. PMSE modulation varies strongly from one cycle to the next~~; they are~~ , being highly variable on spatial scales smaller ~~km and time scales of minutes that are~~ than a km and timescales shorter than the scales assumed for the variation of dust parameters. ~~Averaged~~ Average curves over several heating cycles are similar to the overshoot curves predicted by theory and observed previously. Some ~~individual curves however, show a stronger overshoot than observed~~ of the individual curves show stronger overshoots than reported in previous studies and they exceed the values predicted by theory. A possible explanation ~~for this difference can lie in~~ is that the dust charging conditions ~~that are different during the night or other conditions might~~

~~be at play. We observe two possible instances of sporadic E-layers that are influenced by heating but do not show overshoots, as is to be expected~~are different either because of the reduced solar illumination around midnight or because of long-term changes of ice particles in the mesosphere. We conclude it is not possible to reliably derive the dust charging parameters from the observed PMSE modulations.

1 Introduction

Polar mesospheric summer echoes (PMSE) are strong, coherent radar echoes observed from altitudes of 80 to 90 km at high and mid-latitudes during the summer. It was first noted in the 1970s that these coherent radar echoes were unusually strong (Ecklund and Balsley, 1981; Czechowsky et al., 1979); and that they originate from the height of the extreme temperature minimum around the mesopause that occurs at high and mid-latitudes in the summer months (Ecklund and Balsley, 1981). Later, the echoes were observed from various locations using radars with frequencies ranging from 50 MHz – 1.3 GHz (Cho and Röttger, 1997). The PMSE is observed from mid-May to the end of August in the northern hemisphere, with the main occurrence during local noon (Latteck et al., 2021).

The observed reflection of the radio waves results from strong variations in the electron density and, thus, the refractive index. The echoes are strong because the backscattered radio waves interfere constructively when the distance between the scattering centers is half the radar wavelength, called the Bragg condition. Scattering at the Bragg condition is typically caused by neutral turbulence in the atmosphere. PMSE echoes arise from a combination of neutral turbulence and the presence of charged ice particles that form near the cold mesopause and influence the electron distribution; the presence of these ice particles expands the Bragg scales for which the echoes are observed (Rapp and Lübken, 2004). The spatial distribution of the ice particles at these altitudes is influenced by the complex neutral atmosphere dynamics caused by the upward propagating gravity waves. It can also be seen in the structure of Noctilucent clouds (NLC) (Dalin et al., 2004).

The region of PMSE occurrence overlaps with that of NLCs, an optical manifestation of these ice particles. Temperature studies of the summer Arctic mesosphere suggest that both phenomena are temperature controlled and occur at temperatures 150 K and lower around the mesopause (Lübken, 1999) where water ice particles can form. Since 2007, the water ice particles have also been observed by satellites in so-called polar mesospheric clouds (PMCs); the optical properties of water ice explain the measured cloud extinctions with inclusions of smaller meteoric smoke particles (Hervig et al., 2012). The meteoric smoke particles are nanometer-sized dust particles that form from ablated meteoric material in the altitude range 70 – 110 km (Rosinski and Snow, 1961; Hunten et al., 1980; Megner et al., 2006). The satellite observations also support the existing hypothesis that the ice particles are formed by heterogeneous condensation, which has recently been supported by a study that applies a new theoretical condensation model (Tanaka et al., 2021). The surface charging of dust particles, be it meteorite smoke, ice particles, or a mixture of both, is a necessary process that influences the growth of ice particles and, at the same time, gives clues to their size and composition (Rapp and Thomas, 2006). The dust can, for example, become negatively charged from electron attachment in the PMSE altitude range. This is indicated by rocket measurements of so-called electron bite-outs (depletion in electron density) where PMSE is present (Rapp and Lübken, 2004) (and references therein).

Previous works have shown that the modulation of PMSE during artificial heating with HF radio waves could be used to study the underlying plasma and dust particles (Biebricher et al., 2006; Mahmoudian et al., 2011, 2020). During such heating experiments, the electron temperature is locally and temporarily enhanced (Rietveld et al., 1993); and Chilson et al. (2000) first noticed that PMSE can be modulated during such heating. The PMSE often almost disappears when the heater is turned on and then returns when the heater is turned off again. It is assumed that the increased electron temperature during heating and the resulting increased diffusion reduces the fluctuations in the electron density and thus the PMSE power (Rapp and Lübken, 2000). Havnes (2004) found that with an adequate on/off time of the heater, a so-called overshoot characteristic curve could be generated, in which the PMSE power did not return to the original value after heating but exceeded it. Such overshoot curves have been observed in many simultaneous radar and heating studies of PMSE made with EISCAT. The overshoot curves have also been observed for some Polar Mesospheric Winter Echoes (PMWE) (Kavanagh et al., 2006; Belova et al., 2008; Havnes et al., 2011). Most PMWEs do not appear to be associated with the presence of dust (Latteck et al., 2021). Still, those showing overshoots are more likely related to the presence of small dust particles, possibly meteoric smoke.

With this work, we want to investigate whether and how the PMSE modulation during heating can be used for systematic investigations of the charged dust component. We present observational studies of PMSE with the EISCAT VHF radar during four VHF/Heating campaigns, all done in August during twilight or night conditions. This is the first systematic investigation of PMSE modulation under reduced sunlight conditions and toward the end of the PMSE season. The remaining manuscript is structured as follows: First, section 2 introduces the PMSE modulation during heating and the overshoot effect. Section 3 describes the experiments we performed, including the radar and heating parameters, and gives an overview of the observational results. Then a discussion of the PMSE modulation is given in section 4 where we first discuss the cases of quiet ionospheric conditions and of an ionosphere that is moderately influenced by energetic particle precipitation and then give an overview of the observed PMSE modulation. We make a comparison with a model calculation and discuss the overall outcome. A short conclusion is given 2, and additional information on observational data is provided in the appendix and supplementary material.

2 PMSE and Heating

The EISCAT Heating Facility transmits high-frequency radio waves of high power into the atmosphere (Rietveld et al., 1993). Electron oscillations associated with wave absorption translate into thermal motion, heating the electron component while the other plasma components keep their initial temperature. As mentioned above, it was found that this active heating influences the PMSE signal. During the experiments, the heating is switched on and off in pre-defined time intervals (48 seconds on and 168 seconds off). The PMSE echoes

are simultaneously observed with the EISCAT ~~VHF~~ radar. The time variation of the observed PMSE power is sketched in

95 Fig. 1 to illustrate the observed phases of the PMSE heating cycle and the often seen overshoot curve: decline, heating phase, recovery/overshoot, and relaxation.
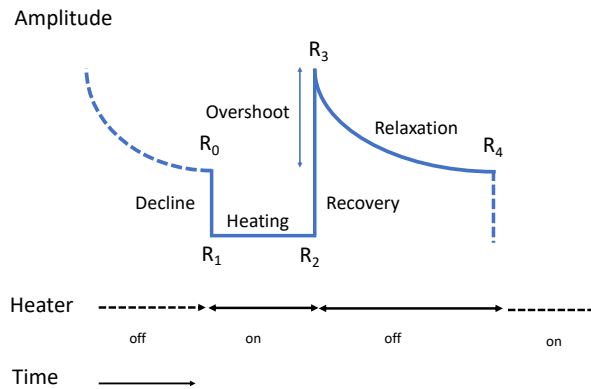
Figure 1. Sketch of the PMSE modulation due to HF heating in a typical overshoot curve; the power amplitudes during different times of the heating cycle are defined.

The amplitudes (R_0, R_1, R_2, R_3 and R_4) marked in Fig. 1 will be considered in our analysis of the observations below, where R_4 is then the start (R_0) of the next subsequent cycle. We follow previous studies (e.g. (Havnes et al., 2015)) and refer to the curves that describe the measured PMSE during one heating cycle (On and Off time) as overshoot curves.

100 **Decline** - $R_0 \to$ ~~R_{T0}~~ $\to R_1$: As the heater is switched on at R_0, the power effectively falls off instantaneously (depending on the radar frequency used) (Havnes, 2004). The back-scattered power drops because the heating enhances the electron temperature and ~~consequently~~, consequently, the electron diffusivity so that the large electron density gradients are reduced ~~and therefore~~. Therefore the backscatter is less efficient (Rapp and Lübken, 2000).

Heating - $R_1 \to R_2$: During the heater on phase from R_1 and R_2 there are some variations in the power amplitude. Because

105 of the higher electron temperature, the charging electron flux on the dust particles increases during the heater on period, and often an increase in the power can be seen. The charging timescales become shorter and compete more with the faster electron diffusion (Mahmoudian et al., 2011).

Recovery/overshoot - $R_2 \to R_3$: The power then increases when the heater is switched off (recovery), and in many cases, the power rises above the previous undisturbed level (overshoot). ~~When the heater is switched off again, the~~ The electron

110 temperature drops quickly to the initial value before the heater ~~was~~ is on due to the highly collisional regime ~~present~~ at these altitudes. The dust particles carry a higher charge than before and ~~therefore~~ repel the electrons more strongly. The electrons follow the ion diffusivity, and as a result, the electron density gradients ~~are largerthan initially and therefore the backscatter is higher~~ become larger. This causes the backscatter to be larger, creating an overshoot in ~~the~~ power.

Relaxation - $R_3 \rightarrow R_4$: ~~During the next phase the~~ Now the power relaxes back to the previous undisturbed level. ~~With~~, with a varying relaxation time depending on the conditions. With a long relaxation time, new and undisturbed plasma can enter the radar beam, or the dust present has time to ~~decharge~~ discharge (Havnes, 2004).

~~The amplitudes (R_0, R_1, R_2, R_3 and R_4) marked in Fig. 1 will be considered in our analysis of the observations below, where R_4 is then the start (R_0) of the next subsequent cycle. We follow previous studies and refer to the curves that describe the measured PMSE during one heating cycle (On and Off time) as overshoot curves.~~

3 Observations

We first describe the overall observation conditions, radar ~~operation~~ operations, and radar analysis and present an overview of the data.

3.1 Overall observation conditions

The presented observations were carried out during the "Mesoclouds 2018" and "Mesoclouds 2020" campaigns ~~conducted in a collaboration between~~ in collaboration with UiT Tromsø and IRF Kiruna. The EISCAT VHF radar and the EISCAT Heating ~~facility~~ Facility are located in Ramfjord near Tromsø, Norway (69.59°N, 19.23°E). The observations were made on 11/12 August 2018, 15/16 August 2018, 05/06 August 2020, and 06/07 August 2020, ~~respectively~~ during the night between 20:00 and 02:00 UT. ~~Most observations of PMSE and heating have been done around noon and often during high summer, June and July.~~ These observations thus represent dusk and night conditions with reduced influence of sunlight on the observational volume compared to other observations~~. We estimated the relative difference an observation done on 21 of June (summer solstice) at noon receives of sunlight compared to our observations for 11 and 15 of~~, mainly done around noon in June and July.

The solar zenith angles during the observations are in the range of 88-97 degrees, where the sun is below the horizon for all angles above 90 degrees. PMSE at 80-90 km altitude are still sunlit but to a lesser extent for most of the previous PMSE observations. To estimate the difference we compare the solar illumination at the time of our 15 August (2018) ~~at 21h and 22h (UT) (see e. g Giono et al. (2018) for how this can be done). Where we used solar flux for the~~ observations to those of the summer solstice in the same year. We derive the solar UV flux by calculating the absorption of the solar UV flux by O_2 along its path through the atmosphere (described by(Giono et al., 2018). We use solar Lyman-α line (121.56 nm) flux from the SOLSTICE instrument on the SORCE satellite (https://lasp.colorado.edu/home/sorce/data/ssi-data/) and ~~neutral density for~~ O_2 densities from the NRLMSISE-00 Atmosphere Model (Hedin, 1991) for the location of the EISCAT VHF radar. We estimate that the solar ~~illumination~~ photon flux in August at PMSE altitudes is reduced by at least one order of magnitude ~~in comparison to the observation~~ compared to noon conditions in June~~during the day. This influence should translate~~, as seen in Fig. 2. This influence translates to a reduced photo-emission current ~~and thus influence~~ by an order of magnitude. It thus influences the dust charging conditions since the photo-emission current is proportional to the photon flux (Mahmoudian et al., 2018).
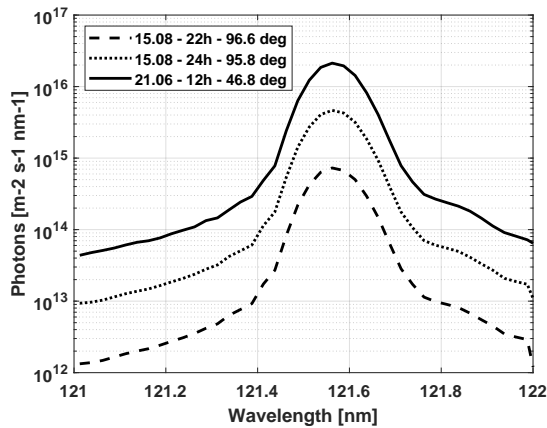
Figure 2. Estimated photon flux for the Lyman α line for 21.06 at 12h (UT) and 15.08 at 22h and 24h (UT) at 85 km altitude. Solar zenith angles used in the estimation included in the label are from the IRI model (2016)

145   Simultaneous optical measurements of NLC were done using two optical NLC cameras located at Kiruna and Nikkaluokta (Sweden). Both locations of the NLC cameras are about 200 km, about 200 km south of Tromsø, which permits making NLC triangulation measurements). There was however, however, no NLC observation above the radar site, mainly because of weather conditions. There was bad weather on 11/12 August (clouds) both in Kiruna and Nikkaluokta. During the night of 15/16 August, faint NLC NLCs were observed from Kiruna close to the horizon, approximately above Andøya, i.e., more
150   westward than the EISCAT site. Weather conditions prohibited NLC observations during the 2020 radar campaigns.

        Fig. 3 a and b (a) and (b) show the temperature profiles (blue line) as measured by the Aura satellite and frost point temperature profiles (green line) estimated using the Aura water vapor data (both the temperature and water vapor were measured with the Microwave Limb Sounder, MLS instrument). These profiles have been selected to be closest ones to the radar location and to the times of the PMSE observations. The height ranges in which the temperature is lower than the frost point temperature
155   indicate the regions where ice particles can form. This gives a good indication of the conditions present in the atmosphere, showing that the temperatures are cold enough to facilitate ice particle formation at PMSE altitudes, however. However, there could be variations due to the spatial and temporal difference differences between the measurements that must be kept in mind. These measurement points were the closest in time and space to the PMSE observations; the horizontal distance to Tromsø is about 490 km in Fig. 3 (a) and about 293 km in Fig. 3 (b).
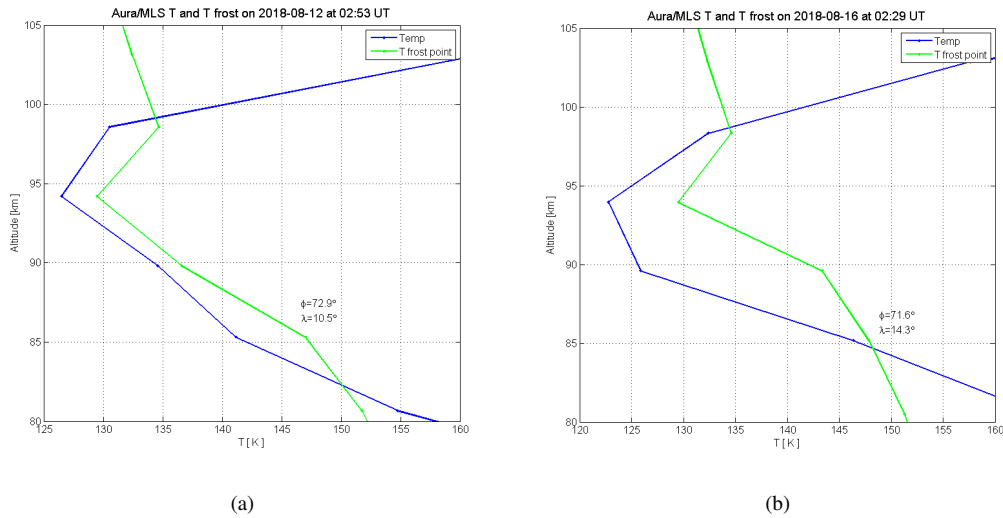
Figure 3. Temperature profiles (blue line) as measured by the Aura satellite at 12.08.18 and 16.08.18, and frost point temperature profiles (green line) estimated using the Aura water vapor data. ~~Closest measurements~~ Latitude and longitude of the measurement points are given in ~~space~~ the figures by ϕ and ~~time.~~ λ respectively

3.2 Radar operation and data analysis

The radar observations were made in the zenith direction with the EISCAT VHF (224 MHz) antennas near Tromsø (~~69.5864°N, 19.2272°~~69.59°N, 19.23°E). The radar code used was Manda, and reference to EISCAT documentation Tjulin (2017) and radar and heating system parameters are given in Table 1. The EISCAT Heating Facility (Rietveld et al., 1993, 2016) was operated with a vertical beam at 5.423 MHz with a nominal 80 kW per transmitter which corresponds to Effective Radiated Power (ERP) in the range between 500 and 580 MW, and X-mode polarization ~~were~~ was used with a sequence of 48 s on and 168 s off. The vertical extension of the heater beam extends far beyond the region covered by the radar. Given that the vertical winds and velocity fluctuations of the PMSE observed with EISCAT VHF are within few m/s and horizontal winds possibly few 10 m/s (Strelnikova and Rapp, 2011), the radar at all times measures PMSE that are influenced by the heating.

A standard incoherent scatter analysis, GUISDAP (Lehtinen and Huuskonen, 1996), was used to derive the radar data products. It provides the electron density derived from the incoherent scatter spectrum, and a value proportional to back-scattered power for the coherent scatter of the PMSE. We~~therefore~~, therefore, use the unit of equivalent electron density as was done previously for observations of PMWE (Kavanagh et al., 2006; Belova et al., 2008) and PMSE (Mann et al., 2016). This equivalent electron density is just the backscattered power multiplied by some constant. In turn, the backscattered power is proportional to $1/(1 + T_e/T_i + \alpha^2)$ as is shown by Pinedo et al. (2014), indicating that when the heater is turned on, T_e increases and consequently the backscattered power decreases. The post-experiment integration time used throughout this analysis was 24 s for computational reasons except for one of the observations when we compare with simulations~~, then a~~. A

resolution of 4.8 seconds was used. We found that choosing a higher time resolution for the overall discussion did not result in additional information. ~~We consider the back-scattered power in units of equivalent electron density throughout this paper.~~

Table 1. Parameters for EISCAT VHF radar operation and EISCAT heating facility. Half of the VHF ~~radar~~ antenna is used for transmitting, and the entire ~~radar~~ antenna is used for receiving(~~beam width~~ beam-width adjusted accordingly)

EISCAT VHF			
Frequency	224.4 MHz	Resolution in range	360 m
Wavelength	1.34 m	System Temperature	240 – 370 K
Transmitter peak power	1.5 MW	Antenna gain	43 dBi
Radar Code	Manda	Half-power beam width	1(2) x 2.4 x 1.7 °
EISCAT Heating Facility			
Frequency	5.423 MHz	ON time	48 s
Beam Width	7 °	OFF time	168 s

3.3 Overview of observations

The observations were made from 20:00 to 02:00 UT ~~during~~ on four nights in August 2018 and 2020. The observations are displayed in Fig. 4 shown for the entire ~~time~~ period and with altitudes from $80 - 110$ km. ~~This altitude range allows us to show the PMSE present as well as other relevant information, like particle precipitation and possible sporadic E-layers,~~ hence including PMSE and the conditions of the surrounding ionosphere. White vertical areas are observation gaps due to ~~operation problems. In each data set we~~ operational problems. We identified interesting measurement intervals ~~that~~ in each data set we considered for analysis. A closer look at each area is given in ~~Appendix A as well as~~ a supplement to the paper, and an overview of the time and altitude range of the areas ~~are given~~ is shown in Table A1 in the appendix.
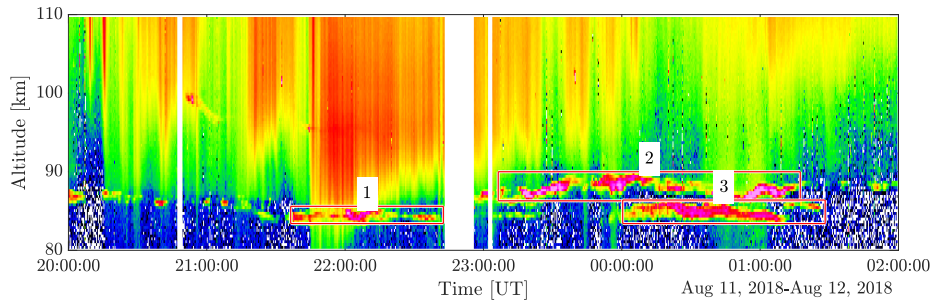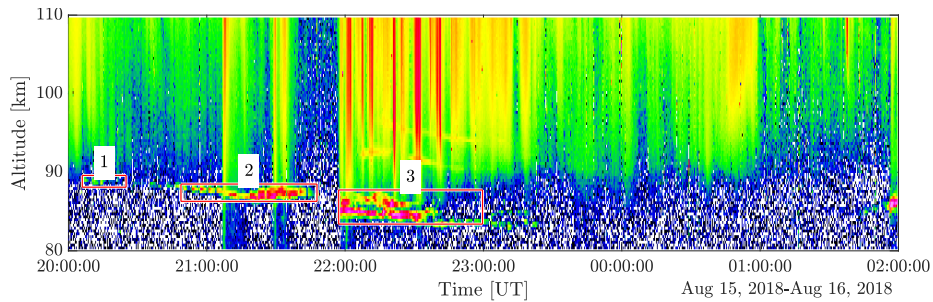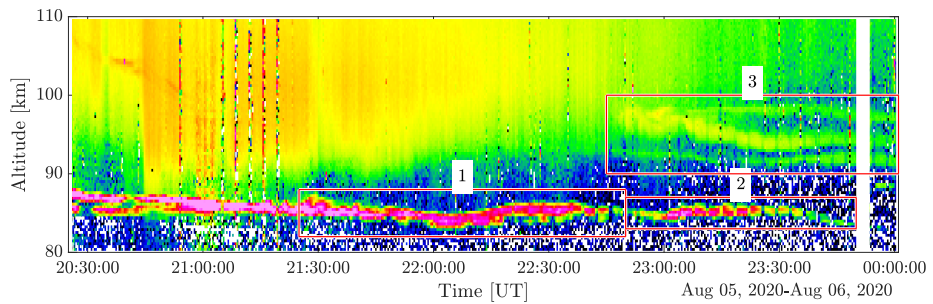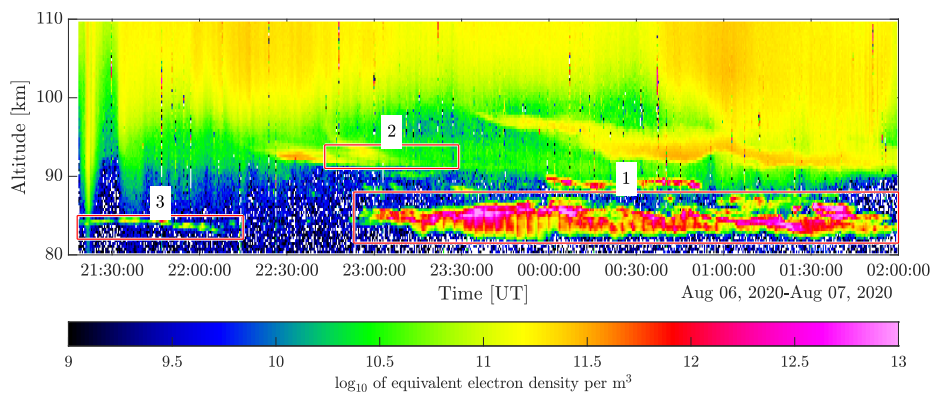
Figure 4. Overview of all four observation days with time intervals and dates given in each respective figure.

Observation 1: 11/12 August 2018 ~~During the first night PMSE were~~ PMSE was observed until around 01:30 am. One can see that the electron densities above and partly below the PMSE are high, showing the typical appearance of particle precipitation. In area 1, the precipitation is ~~especially strong~~strong, and enhanced electron density was observed as low as 80 km, well below the PMSE layer. We considered:

- Area 1: PMSE with strong precipitation in the altitude range 83.4 – 85.6 km from 21:36 UT lasting about 20 heater cycles

- Area 2: high altitude and ~~long lived~~ long-lived PMSE layer extending from 86.3 – 90 km during about 40 heater cycles starting from 23:06 UT with some precipitation.

- Area 3: low altitude PMSE at 83.4 – 86.4 km from 00:00 UT lasting about 30 heater cycles with some precipitation at ~~end of~~ the end of the layer.

~~Overview of all four observation days with time intervals and dates given in each respective figure.~~

Observation 2: 15/16 August 2018. ~~During the second observation, PMSE were~~ PMSE was observed before midnight and then again at 2:00 am at the end of the measurements. ~~A~~ The first observed PMSE (Area 1) seems not influenced by precipitation~~, it almost seems that it was triggered by the heating.~~. The PMSE observed later (~~Area~~ Areas 2 and 3) are influenced by moderate precipitation. Modulation is seen in the backscattered power of the lightly ionized portion of the ionosphere from 90-110 km, which can be seen around 20-21 UT. We considered:

- Area 1: high altitude weak PMSE observed around 20:30 UT at 88 – 90 km

- Area 2: PMSE observed from 20:50 UT to 21:50 UT PMSE at 86 – 88 km, in parts influenced by precipitation

- Area 3: PMSE from 22:00 UT ~~PMSE~~ influenced by moderate precipitation extending over altitudes 83.4 – 87.8 km during about 30 heater cycles

Observation 3: 05/06 August 2020. ~~During the third observation, PMSE were~~ PMSE was observed only before midnight. Some ~~of the observations (Area~~ observations (Areas 1 and 2) show no apparent influence of precipitation. Before the start of Area 1, there is PMSE present~~, however~~. However, this is not ~~considered due to operational problems~~included in the analysis due to (most likely) direct interference from the heater caused by arcing and can be seen as vertical lines extending through all altitudes. For completeness, we also consider Area 3, which displays a layered structure and is influenced by the heating. ~~Both, the~~ The height and the shape suggest, however, that this is not PMSE ~~and rather~~ but rather a sporadic E-layer. We considered:

- Area 1: strong PMSE in the absence of apparent precipitation for about one hour from 21:30 UT at 82 – 88 km

- Area 2: PMSE at 83 – 87 km in the absence of apparent precipitation between 22:50 UT and 23:50 UT

- Area 3: structure observed above 90 km from 22:45 UT consistent with a sporadic E-layer. Not included in analysis.

Observation 4: 06/07 August 2020. From the fourth observation, we see a low altitude PMSE layer only slightly influenced by precipitation, a second layer at high altitude influenced by heating that also might be a sporadic E-layer, and a third area extending over a long period in time and many altitudes that ~~does~~ do not seem to be influenced by particle precipitation. We considered:

- Area 1: a long interval of PMSE between $81-88\,$km partly in the quiet ionosphere and partly influenced by ~~electron~~ precipitation

- Area 2: Sporadic E-layer above PMSE height. Not included in analysis.

- Area 3: a weak PMSE with little apparent precipitation for about one hour from 21:30 UT at $82-88\,$km

We find~~in general~~, in general, that the overshoot effect disappears in the presence of strong or moderate precipitation, as ~~can be~~ seen in the 15/16 August 2018 observation ~~for example~~ in Fig. 4. This is better illustrated in the figures given in ~~Appendix A~~ the supplement to the paper, where each area is enhanced. ~~In~~ At the beginning of the observation campaign on 15/16 August 2018 (area 1), a weak PMSE developed under very quiet ionospheric conditions. ~~We speculate that the heating possibly triggered the formation of PMSE in this instance.~~ The echoes are only weakly enhanced in comparison to surrounding areas~~and~~, the back-scattered power is reduced during heating, and also an overshoot is observed (see Fig. **~~?? in Appendix A~~**A4 in the supplement to the paper).

4 Observed PMSE modulation

First~~we~~, we discuss two selected cases, one with little or no particle precipitation and one with moderate precipitation. Then we summarize the heating effect and overshoots visible in all the observations and discuss these findings in the context of previous observations. ~~Then we discuss two selected cases, one with little or no particle precipitation and then one with moderate precipitation. Finally~~Finally, we compare a selected case with simulations of the overshoot cycle and discuss what information we can gain from modulating PMSE with heating.

4.1 ~~Overall observational discussion~~

~~Here we summarize the decline and overshoot ratios from the histograms in Fig. ??-?? in the appendix for all the four observations (3 areas each) shown in Table 2. In general the heating effect is seen in more than half of the heating cycles for each respective area with most of the average ratios showing values close to 0.75. It must be noted that these calculations show only the observations that have a value of~~ $R_0 > 10^{10.5}$ ~~to indicate the presence of PMSE and thus excluding most of the heating cycles that are not influenced by heating like random noise. This however causes the faintest PMSE to be excluded from the histograms like is seen for the overshoot ratio for area 1 from 15 of August 2018, here the PMSE power is below the threshold and thus no cycles are included in the calculation despite 100 % of the cycles showing a decline due to heating. This would suggest that manually inspecting low power PMSE influenced by heating would be a better option or introducing other~~

245 criteria to include these low power observations. This might be true for other observations as well and thus the threshold needs to be reconsidered, either the threshold for considering what is a PMSE is to high or that the heating influence can be seen to have an effect on a layer that normally would not be considered as a PMSE since it most likely is at the threshold of detection for the radar being used and the irregularities are no longer comparable to the radar Bragg scale.

Two observations showed layers at very high altitudes and would not be considered PMSE, where their altitude range is
250 more common for sporadic-E layers. This is Area 3 from 5-6 of August 2020, with altitude extending from around 91 – 98 km , showing 3 distinct layers. And Area 2 from 6-7 of August 2020 (From this observations day there are two large layers of possible sporadic E-layer, however we only focus on the area where clear heating can be seen). Examining the ratios in the table the heater seems to be effective in 66 % of the cases with about 0.75 mean value for those cases with visible heating for 5-6 of August and in 83 % of the cases for 6-7 of August with an average of 0.52 for those cases. This we would expect for a
255 sporadic E-layer as it has been shown before that these types of layers can be influenced by heating (e.g Ignat'ev (1975) with a reduction in received power when the heater is on. For the overshoot ratio the histograms show only 10 % and 17 % of the observations showing an increase after the heater is turned on and thus much more of the cycles are showing a decrease. We do not expect an overshoot to be present when heating a sporadic E-layer and these numbers confirm this. Also the average ratios of those few cycles that show an overshoot are very high, 0.87 and 0.89 respectively, indicating that background variation is
260 more likely the cause for an increase and not an actual overshoot. The sporadic E-layers observed here are generally decreasing in amplitude with time and thus it stands to reason that in general the power received is smaller after the heater is turned off than it was before it was turned on. Ignat'ev (1975) argued that when heating a sporadic E-layer the electron density present in the layer would decrease and the layer would increase in thickness and thus spread over a larger area causing a reduction in power.
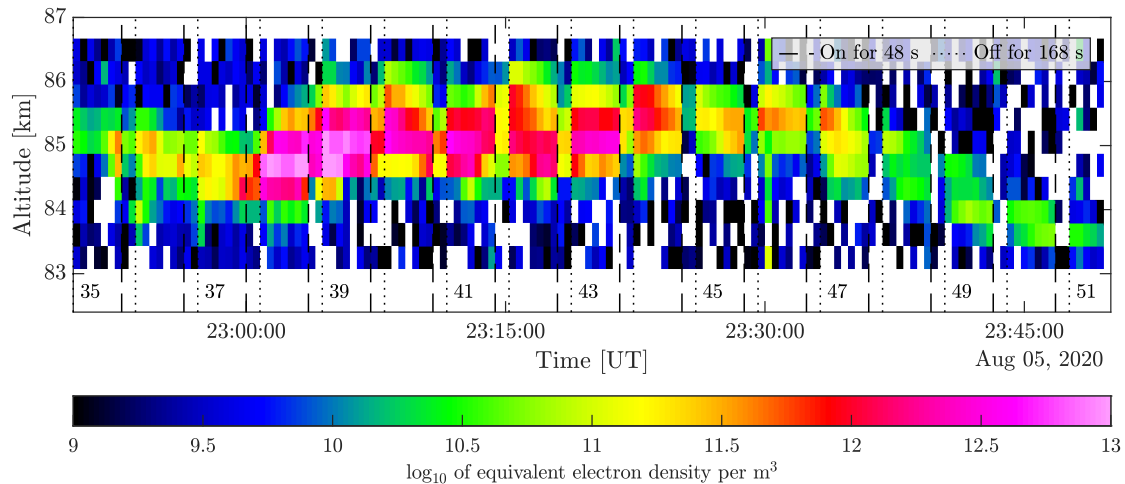
06, 2020, in Area 2.

To summarize; we see only overshoots in less than half of the cycles with many cycles often more influenced by background ionospheric conditions that might overshadow the heating of the PMSE. Ullah et al. (2019) show a larger occurrence of overshoots in their observations, with around 40-70 %, where their observations were during daytime. However in our case we see a few instances where the overshoot in some cycles are unusually large. Myrvang et al. (2021) found that a higher electron temperature due to heating could be achieved during night time compared to daytime which might help explain some of these large overshoots. However Kassa et al. (2005) found for their observations that the heating temperature effect observed increased for the observation with the most amount of sunlight (near noon).

Biggest obstacle in comparing with other observations done during midday are the different on intervals observed during the night of August 05/off times of the heater used in various observations as well as different criteria used in the data analysis and cycle averaging. Other possible reasons for unusually large overshoots could be a change in the PMSE/NLC season as is noted by Latteck et al. (2021) that the season in getting longer and since our observations are at night and close to the end of the season there might be more varying background conditions influencing our observations than those during the day in

4.1 PMSE modulation under quiet ionospheric conditions

To discuss PMSE modulation under quiet ionospheric conditions, we chose an area with no apparent energetic particle precipitation; we consider area 2 from the Aug 05-06, 2020 observation (Fig. 4 (c)). The overshoot curves can be assessed using the overall power plot shown in Fig. 4.1. The beginnings of new heating cycles are marked with dashed lines when the heater is turned on. The dotted line indicates the time when the heater is turned off again. In many cases, the PMSE signal changes at the heater on and off time and during the cycles themselves. The PMSE layer lies within the altitude range of 83-87 km with a maximum extension of 2 km at its widest. There are clear indications of reduced PMSE power when the heater is on; in many cases, we can see clear overshoots.

In Fig. 6, we have selected two altitude sections for a closer look, altitude 85.2 and 85.6 km, where we can see overshoots in many of the cycles. In general, the overshoots are relatively large, with some an order of magnitude larger than the pre-heater value and some showing no apparent increase in the PMSE power after heater turn-off. This seems especially true for the top altitude where the PMSE power is at its highest, the lower height has a somewhat lesser PMSE power, and more overshoots are visible. The decline is visible in many of the cycles and is very strong for cycles 40-47. One can also see that characteristics of decline and overshoot often change between adjacent heating cycles and height intervals, for example, in heating cycle 41.
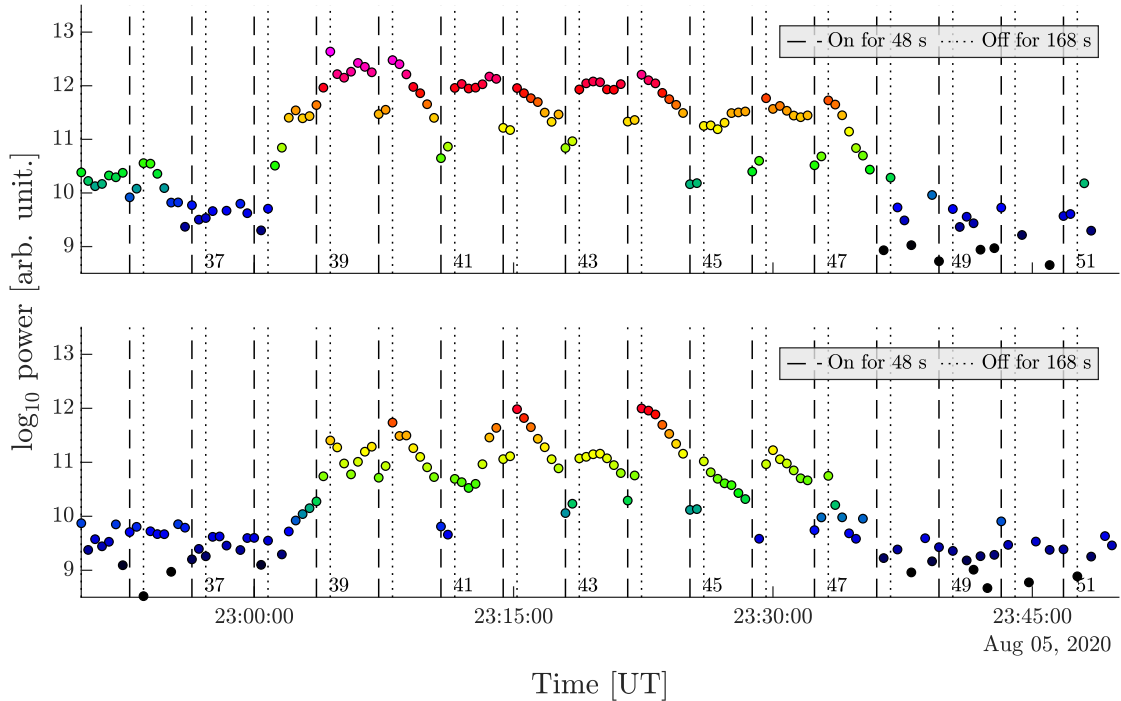
Figure 6. Back scattered power at altitude 85.2 (lower plot) and 85.6 km (upper plot) and heating intervals observed during the night of August 05/06, 2020 in area 2. The ~~colour~~ color of the dots ~~follow~~ follows the ~~colour~~ color scale of Fig. 4.1

For a closer investigation, we describe the ratios of the amplitudes during the different phases of the heating cycle. The different power amplitudes are marked in the overall sketch given in Fig. 1~~: R_0 amplitude before heater on, R_1 amplitude after heater on, R_2 amplitude before heater off, R_3 amplitude after heater off, R_4 amplitude after decline. The R_4 corresponds to R_0 of the subsequent heater cycle. The~~. The different amplitudes observed during the heating cycles ~~for the observation in question~~ are plotted in ~~Figure 7~~Fig. 7, where the amplitude ratios are considered. We find that during most heating cycles, the signal drops when the heating is switched on (decline $R_1 < R_0$, Fig. 7 (a)).

We assume that the observed signals are PMSE when ~~they exceed a value of 10.5 in the given scale (logarithm of the equivalent electron density per m^3~~ $R_0 > 10^{10.5}$ (which corresponds to around 3.16e+10 m^3 ~~)~~(Ullah et al., 2019)), and one can see that in ~~many cases that fall out of range of this condition~~ most cases that do not meet this requirement, there is no PMSE modulation ~~seen, however~~ visible. However, as we will see later, this condition removes a few ~~cases of low power modulated PMSE as well~~instances of low-power modulated PMSE with large overshoots. The same can be said for the green points that show a decline but are below the threshold~~that they could too~~. They could also be showing a decline but ~~in fact~~ be noise due to random fluctuations from the two measurement points.
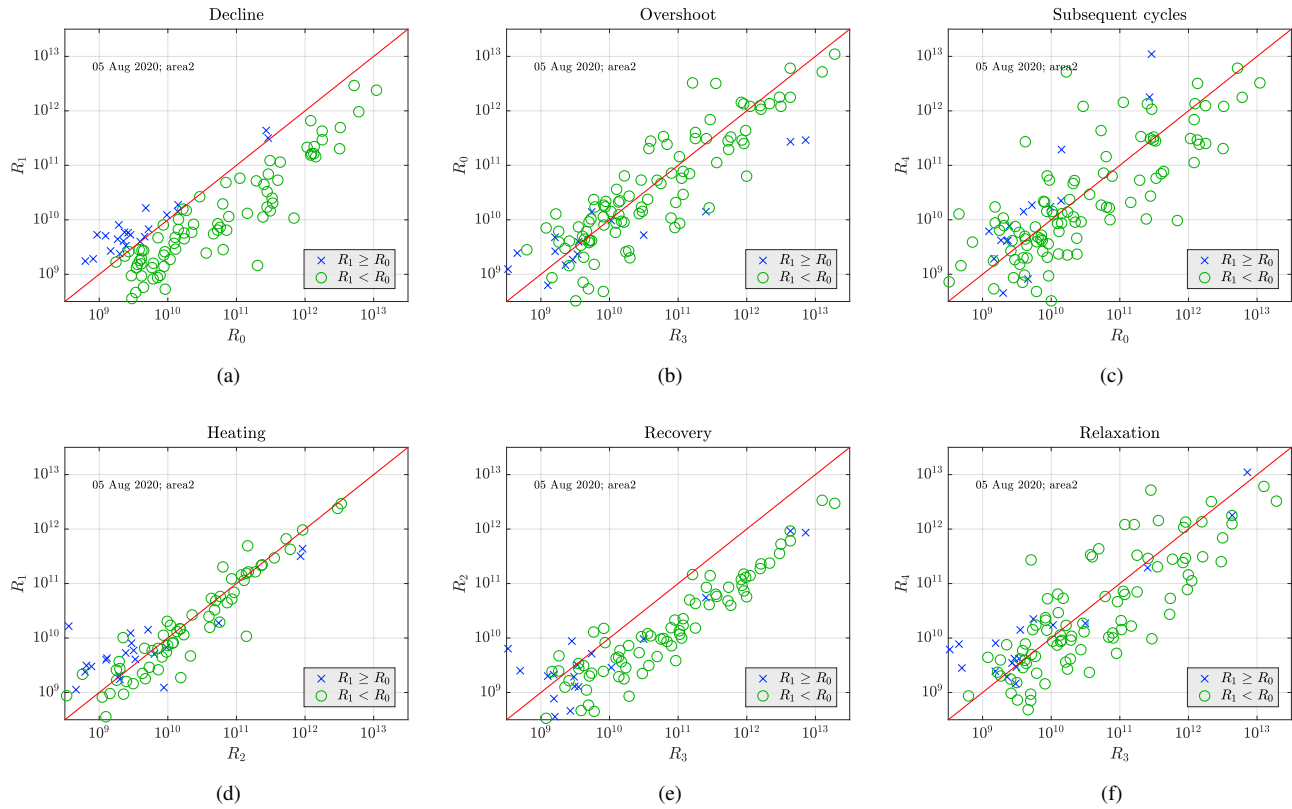
Figure 7. Comparison of the power amplitudes observed on ~~the~~ 5/6 August 2020 ~~in~~, area 2.

The ratio of the amplitudes R_0 and R_3 describes ~~the overshoot , when~~ an overshoot ($R_0 < R_3$), and this comparison shows that overshoots and undershoots are equally abundant independent ~~from~~ of the signal strength (Fig. 7 (b). Comparing the signals at the beginning of subsequent cycles (Fig. 7 (c) shows no trend and a broad range of values which suggests variation either due to ionospheric conditions or due to neutral turbulence (rather than dust).

One can see in Fig. 7 ~~d~~ (d) that for strong signals, the amplitude stays constant or decreases slightly during the ~~heater on~~ heater-on phase. The change of amplitude during the heating can ~~possibly~~ indicate the charging process of the dust particles~~. Where~~, where the faster timescale of diffusion or dust charging dominates (Mahmoudian et al., 2011). According to Havnes et al. (2015) large PMSE structures can cause the diffusion timescale to be longer and consequently, a quicker and larger increase in power during the heater-on phase. The comparison of R_2 and R_3 in Fig. 7 ~~e~~ (e) describes to what extent the signal ~~increase~~ increases again when the heater is switched off. This increase is seen in most cases except for the small amplitudes, ~~these~~ which might be either ~~very low power~~ low-power PMSE or random fluctuations.

Finally, in Fig. 7 ~~f~~ (f), the ratio of R_3 and R_4 describes the signal after the heater is switched off ~~again. Point below the diagonal would describe the decline to normal conditions after an overshoot. Points close to the diagonal would describe that signals are more constant in time.~~ (relaxation). One can see a broad scatter symmetrically around the diagonal, indicating that

the natural variations in the PMSE power are dominant. Any relaxation after heating is difficult to discern from this since their contribution could disappear due to a significant background increase in PMSE power. This is due to the considerable period between the two points (168 seconds), which according to Havnes (2004), is enough time for the ionosphere to change or dust to become discharged, whereas 48 seconds used for the on time is not.

We compile these results in histograms of the amplitude ratios (Fig. 8). The histograms contain only cycles with a value $R_0 > 10^{10.5}$ of the PMSE amplitude before the heater is turned off to only include those with PMSE and exclude the cycles that contain noise or are mostly noise. We only include those cycles that show a decline due to heating in all the histograms. In Fig. 8 (a), we see that 55 % of the ratios are smaller than 1, and thus show a decline (affected by the heater) and that the average value of those ratios that are below 1 has a value of 0.72. This is a reduction of 28 % of the pre-heater value on average when the heater is turned on. We have the overshoot in Fig. 8 (b). Only 10 % of the cycles show an overshoot with an average value of 0.44. Even though there are not many overshoots for this observation, those observed show an average reduction of more than half, indicating very large overshoots. Fig. 8 (c) shows that most (95 %) of the observations show a decrease in power while the heater is on. Figure 8 (d) shows that 66 % of the cycles show an increase in power when the heater turns off, which is similar to the number of cycles that show a power reduction when the heater is turned on. Then in Fig. 8 (e), we see a general increase in power from cycle to cycle. Thus a general decrease to pre-heater value can not be determined, most likely due to increasing background PMSE dominating the signal and the histogram, where 87 % of the cycles show an increase in power in subsequent cycles. This can be related to why we see so few overshoots in this observation, and that increase in PMSE power is significant for many of the cycles. The overshoot disappears due to background variations.
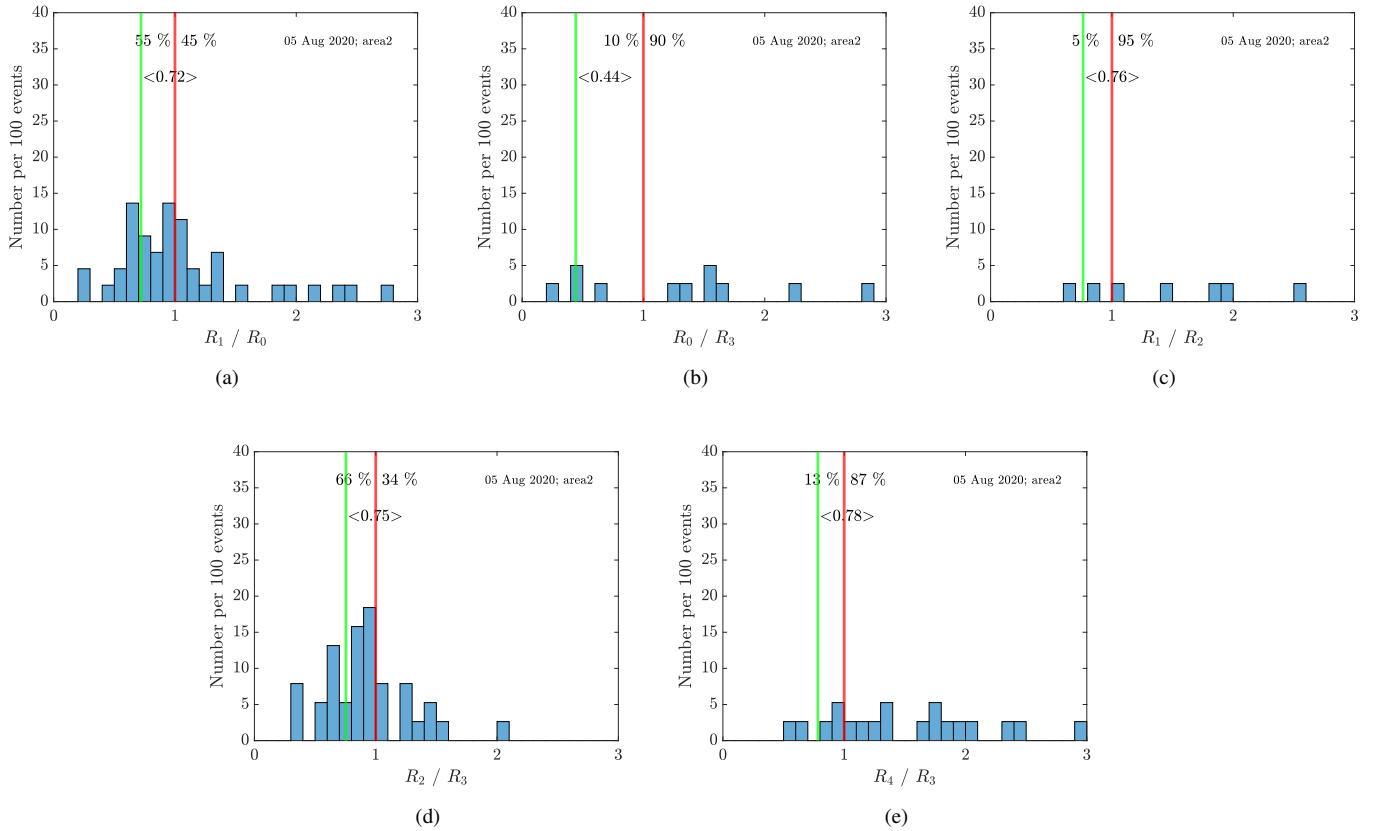
Figure 8. Average of (a) decline, (b) overshoot, (c) heating, (d) recovery, (e) relaxation for the observed data on ~~the~~ 5 August 2020 in area 2. Only overshoot curves with a minimal background amplitude of $R_0 > 10^{10.5}$ are considered. The ratios are chosen ~~in such a way, so~~ that, if we observe an overshoot curve like shown in ~~Figure~~ Fig. 1, all ratios are smaller than 1. Thus, the histograms are clipped at a maximum ratio of 3. The green line and the corresponding number ~~displays~~ display the mean for all ratios smaller than 1.

4.2 PMSE modulation during moderate particle precipitation

Conditions with moderate particle precipitation are observed in Area 2 of the observation ~~made during the campaign on~~ from Aug 15/16, ~~2018.~~ 2018 (See 4 (b)). The overall power plot is shown in ~~Figure~~ Fig. 9. As ~~in the other area previously~~ discussed above, ~~there are~~ some heating intervals ~~with~~ have noticeably very strong overshoots (14,15,16,17). One can note that the

335   influence of the heating is most pronounced ~~in~~ at the beginning and the very end of the observation interval when there is no apparent particle precipitation. Precipitation ~~is clearly present~~ occurs in cycles 18 and 19 and then in cycles 24 and 25. ~~Here when~~ When the heater is switched on, there is no reduction in power, and the precipitation dominates the received signal for all altitudes in these cycles. The power plot for two selected height intervals shown in Fig. 10 shows this in ~~a more detailed way. Where the modulation fully~~ more detail, where the modulation entirely disappears in the cycles influenced by precipitation.

340   This is to be expected and has been shown before, ~~one~~. One of the reasons why the modulation disappears in the PMSE layer

is that the atmosphere below the layer is ionized due to the strong precipitation, and the HF radio wave might be strongly absorbed before it reaches the PMSE layer and thus not be strong enough to ~~appreciably~~ heat the electrons appreciably in the layer.
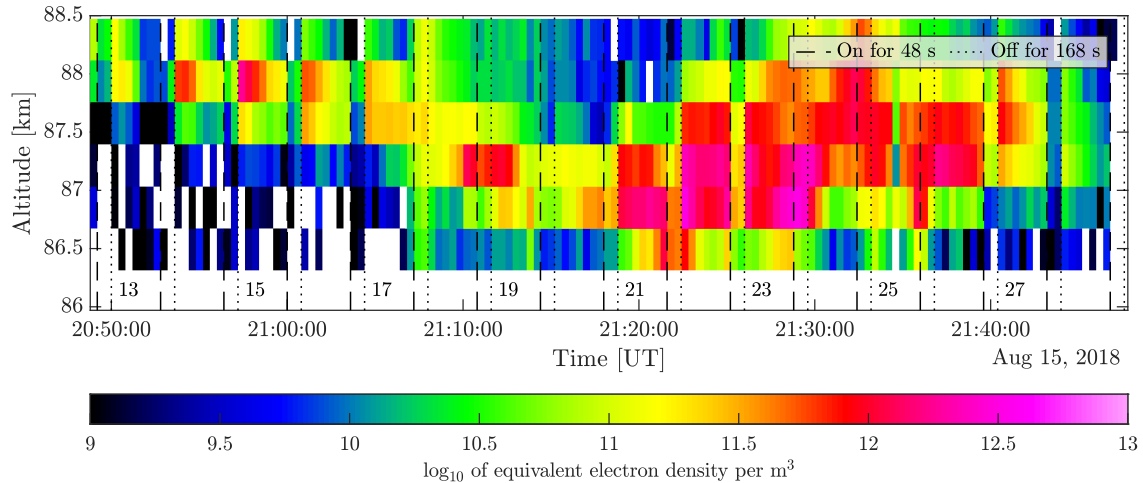
Figure 9. Back scattered power as a function of altitude and heating intervals observed during the night of August 15/16, 2018, in Area 2.

The different amplitudes observed during the heating cycles in this area are plotted in ~~Figure~~ Fig. 11. We find that during most heating cycles, the signal drops when the heating is switched on (decline, Fig. 11 ~~a~~(a)). The cases that show no decline are spread over all amplitudes, indicating the cycles that might be influenced by precipitation and thus might show an increase in power when the heater is on. The overshoots and undershoots are equally abundant independent ~~from~~ of the signal strength (Fig. 11 ~~b~~(b)). As observed in the area discussed above, there is no trend when comparing the signals at the beginning of subsequent cycles (Fig. 11 ~~e~~(c)). The change of amplitude during the heating (Fig. 11 ~~d~~(d)) is small for most ~~of the observations.~~ observations.

In most cases, the amplitude increases (Fig. 11 ~~e~~(e)) when the heater is switched off, similar to the ~~cycles being heated~~ heated cycles, which is to be expected. Finally, in Fig. ~~(11 f)~~ 11 (f), the ratio of R_3 and R_4 describes the ~~signal after the heater is switched off again, showing somewhat more of the cycles that are influenced by the heating showing~~ relaxation, showing a large spread around the diagonal with somewhat more observations showing a reduction. This large spread can be attributed to the ionospheric variability due to the large timescale of the off time, as was mentioned previously.
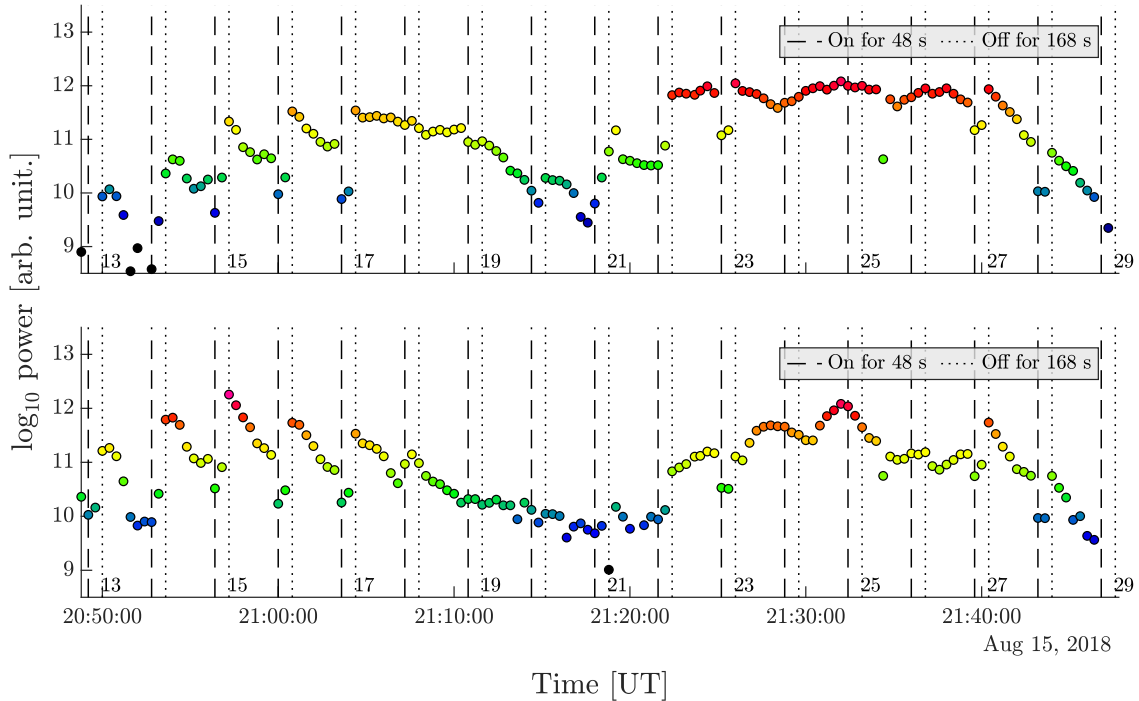
Figure 10. Back scattered power at altitude 87.4(lower panel) and 87.8(upper panel) km and heating intervals observed during the night of August 15/16, 2018 in area 2. The ~~colour~~ color of the dots ~~follow~~ follows the ~~colour~~ color scale of Fig9

The histograms of the power amplitudes are shown in Fig. 12 with the same criterion as before (also given in the figure text). Here the overshoot is seen in 55 % of the cycles with an average of 0.75 decline ratio (Fig. 12 (a), similar to the previous observation. Here the overshoot is seen in 31 % of the observations with an average of 0.64 overshoot ratio (Fig. 12 ~~b). Which (b)),~~ which is more than the previous observation, even with ~~the presence of~~ precipitation. Similar to the previous observation~~we~~
360 ~~see that,~~ when the PMSE power increases ~~in general~~ (and is not influenced by precipitation), we see an influence of the heater but not an overshoot ~~or a very small overshoot~~(or a minimal overshoot). For the cycles with a lower PMSE power (like in cycle 15), the overshoot is large, but the background PMSE power is lower~~and thus~~; thus, the overshoot is easy to see. During the heating, there seems to be a general decrease in the values, with 76 % of the values showing a decrease during ~~heater on~~ the heater-on phase (Fig. 12 ~~e~~(c)). The recovery (Fig. 12 ~~d~~(d)) ratio shows that 58 % has an increase in power when the heater is
365 turned off~~. Showing similar values as~~, showing similar values to those for when the heater is turned on (decline). Then there seems to be a little over half of the cycles that show a general increase in pre-heater values between cycles (Fig. 12 ~~e~~(e)).
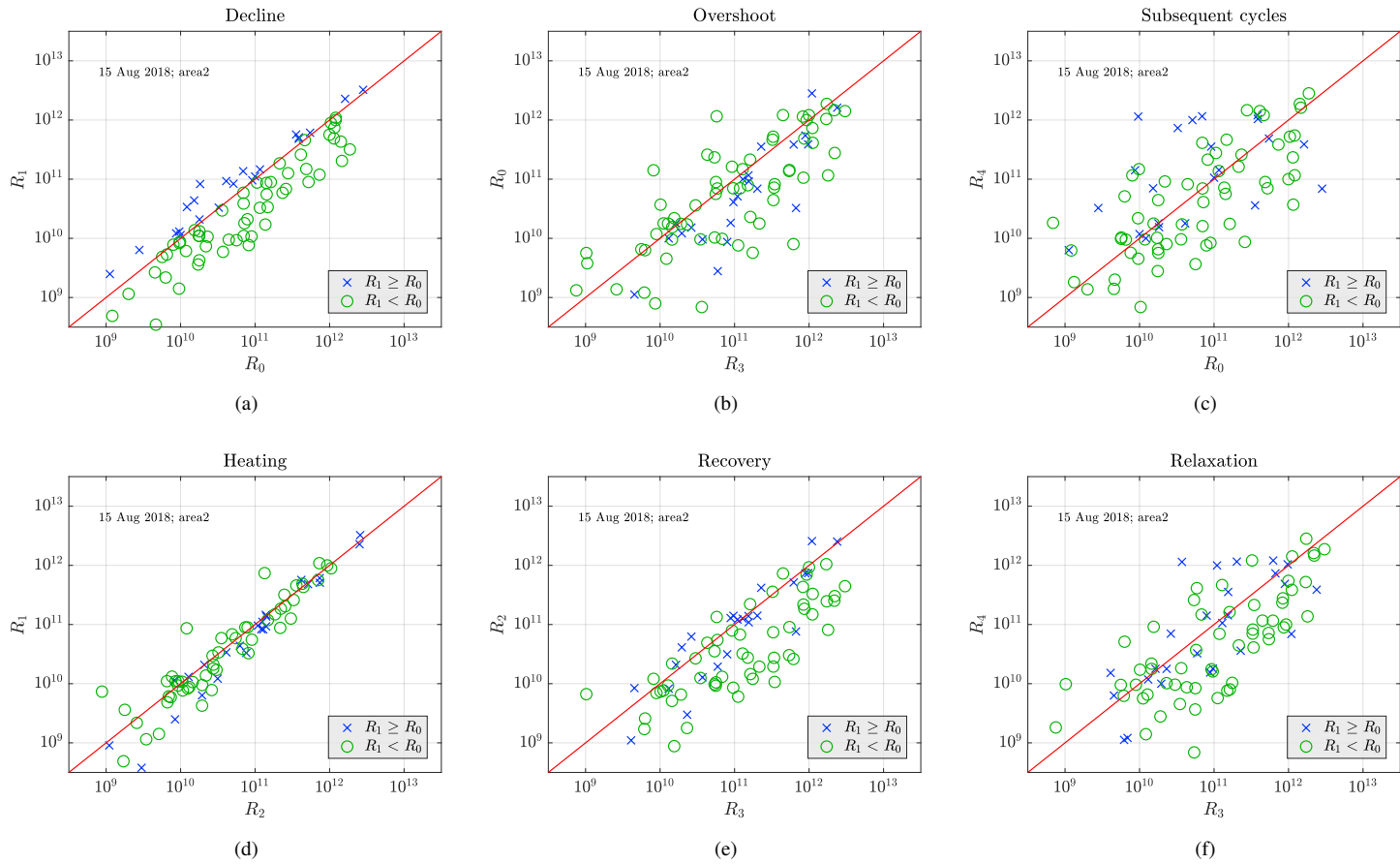
Figure 11. Comparison of the power amplitudes observed on the 15 August 2018 in area 2.
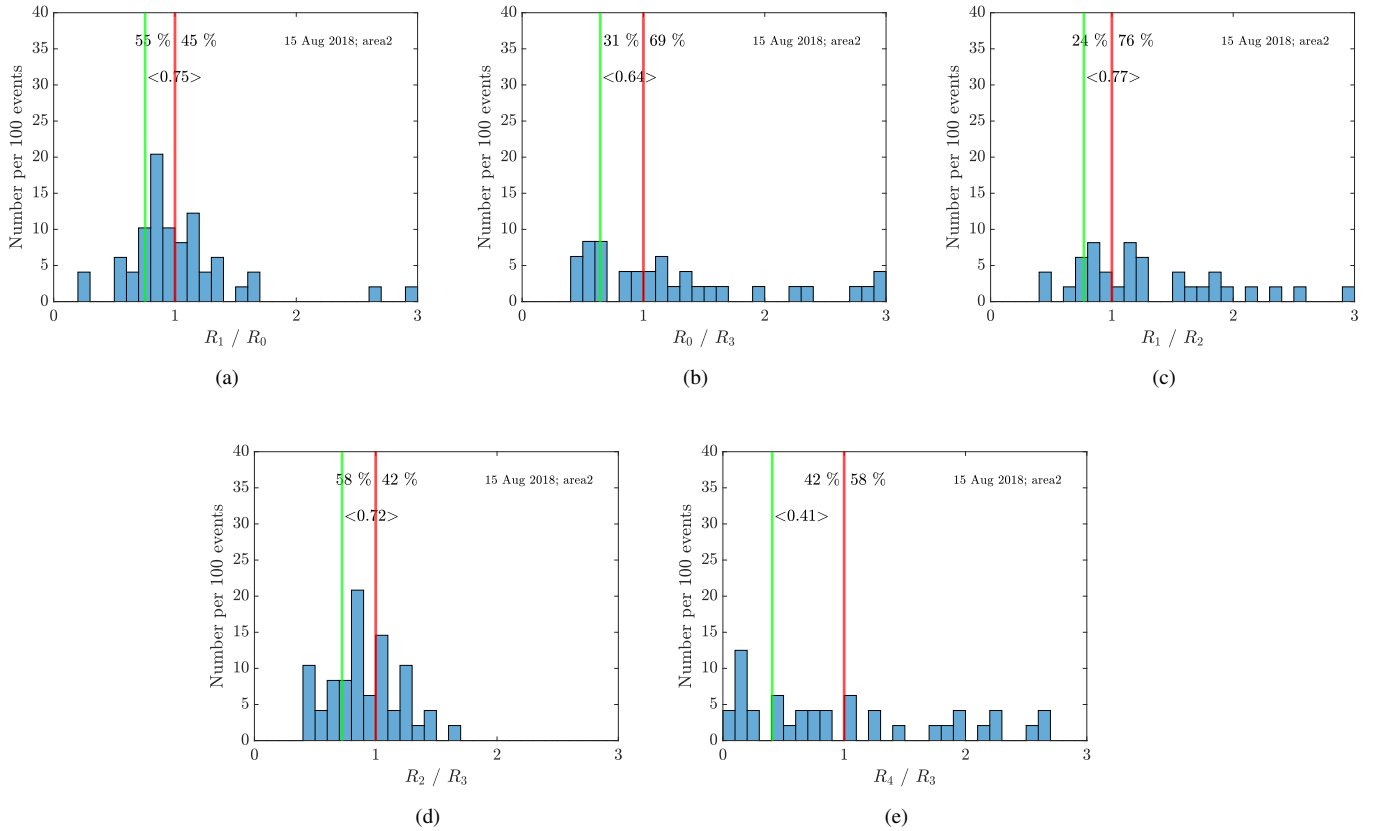
Figure 12. Average of (a) decline, (b) overshoot, (c) heating, (d) recovery, (e) relaxation for the observed data on ~~the~~ 15 August 2018 in area 2. Only overshoot curves with a minimal background amplitude of $R_0 > 10^{10.5}$ are considered. The ratios are chosen ~~in such a way,~~ so that ~~,~~ if we observe an overshoot curve like shown in ~~Figure~~ Fig. 1, all ratios are smaller than 1. Thus, the histograms are clipped at a maximum ratio of 3. The green line and the corresponding number ~~displays~~ display the mean for all ratios smaller than 1.

4.3 Overall observational discussion

Here we summarize, in Table 2, the decline and overshoot ratios for all the observations (See Fig. D1-D4 in the supplement to the paper for reference). In general, the heating effect is seen in more than half of the heating cycles for each respective area,

370 with most of the average ratios showing values close to 0.75. These calculations show only the observations with a value of $R_0 > 10^{10.5}$ to indicate the presence of PMSE and exclude noisy data.

This, however, causes the faintest PMSE to be excluded from the histograms, as is seen for the overshoot ratio for area 1 from 15 August 2018; here, the PMSE power is below the threshold. Thus no cycles are included in the calculation despite 100 % of the cycles showing a decline due to heating. This would suggest manually inspecting low-power PMSE influenced

375 by heating would be a better option or introducing other criteria to include these.

Table 2. Summary of histogram results (see part D in the supplement to the paper) for the decline (R_1/R_0) and the overshoot (R_0/R_3) ratio when they are smaller than 1 (indicating heating effect and overshoot) for all four observations. These numbers only include observations with minimum background amplitude $R_0 > 10^{10.5}$. A1 refers to area 1 for that observation's date and so forth.

	Decline $R_1/R_0 < 1$			
	Overshoot $R_0/R_3 < 1$			
	Average of ratio	% of ratio		
	Average of ratio	% of ratio		
11/12.8.18			A1	
	0.76	58 %		
	0.56	45 %		
			A2	
	0.75	61 %		
	0.57	51 %		
			A3	
	0.77	55 %		
	0.61	50 %		
15/16.8.18			A1	
	0.74	100 %		
		-		
			A2	
	0.75	55 %		
	0.64	31 %		
			A3	
	0.69	63 %		
	0.41	40 %		
5/6.8.20			A1	
	0.72	46 %		
	0.48	44 %		
			A2	
	0.72	55 %		

To summarize, we see only overshoots in less than half of the cycles, with many cycles often more influenced by background ionospheric conditions that might overshadow the heating of the PMSE. Ullah et al. (2019) show a more significant occurrence of overshoots in their observations, with around 40-70 %, where their observations were during daytime. Havnes et al. (2015) observations had a much larger ratio of cycles with decline present and a slightly higher percentage of overshoots present.

However, in our case, we see a few instances where the overshoot in some cycles is unusually large. Myrvang et al. (2021) found that a higher electron temperature due to heating could be achieved during night-time compared to daytime which might help explain some of these large overshoots. However, Kassa et al. (2005) found for their observations that the heating temperature effect observed increased for the observation with the most amount of sunlight (near noon).

Other possible reasons for unusually large overshoots could be a change in the PMSE/NLC season, as is noted by Latteck et al. (2021) that the season is getting longer. Since our observations are in reduced sunlight and close to the end of the season, more varying background conditions might influence our observations than those during the day in June/July.

4.4 Comparison of a selected observation to simulation

Here we take a closer look at the approximate one-hour time interval, which is marked as area 2 in the observation from 15-16 of August 2018, shown in Fig. 13; the data cover the heating cycles 12 to 27 and range over seven height intervals of around 360m each. The ionosphere is influenced by precipitation in cycles 18 and 19 and then again in cycles 24 and 25, and there are no overshoots present in those heating cycles, as mentioned before. The PMSE in intervals marked with A, B, and C in the figure shows a decrease when the heater is on and overshoots when the heater is turned off. Interval A shows relatively low PMSE power but quite high overshoot curves compared to intervals B and C, as we will investigate further.
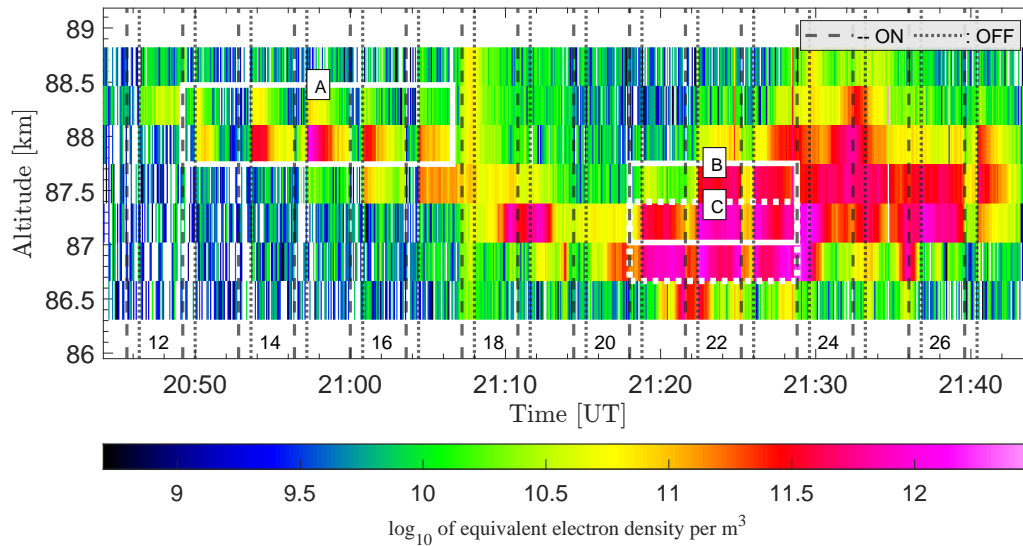
Figure 13. Overview of Area 2 - 15 of August ~~2018. With~~ 2018, with interesting visible overshoot cycles marked with intervals A, B, and C. Data resolution is 4.8 seconds. Cycles are marked in the figure (from 12 to 27) as well as their corresponding On~~and~~/OFF period

Individual heating cycles are shown in Fig. 14 ~~a~~ (a) for both altitudes from interval A, with PMSE power ~~along with~~ and measurement error provided by the EISCAT GUISDAP analysis. ~~Shown~~ The corresponding average overshoot cycle for the respective altitude is shown on the right in Fig. 14 ~~b~~ (b) in blue is the corresponding average overshoot cycle for the respective altitude. As can be seen, the overshoot is ~~rather~~ relatively strong for many of the heating cycles, especially ~~strong overshoot is~~

400 the strong overshoot seen in cycle 15 for both altitudes with ~~rather~~ relatively high but decreasing overshoot on both sides of the cycle. Note the two ~~different~~ y-axis scales for the different altitudes, where the heating cycles from altitude 88 km ~~has~~ have such a low background PMSE power that the scale is an order of magnitude lower than the altitude below. Both altitudes have relatively low background PMSE power compared to intervals B and C, ~~where the cycles~~ with the PMSE at 88 km altitude ~~the PMSE is~~ barely present or the irregularities on the limit of being seen by the VHF radar. It is thus interesting to find such large

405 overshoot cycles for this particular interval.
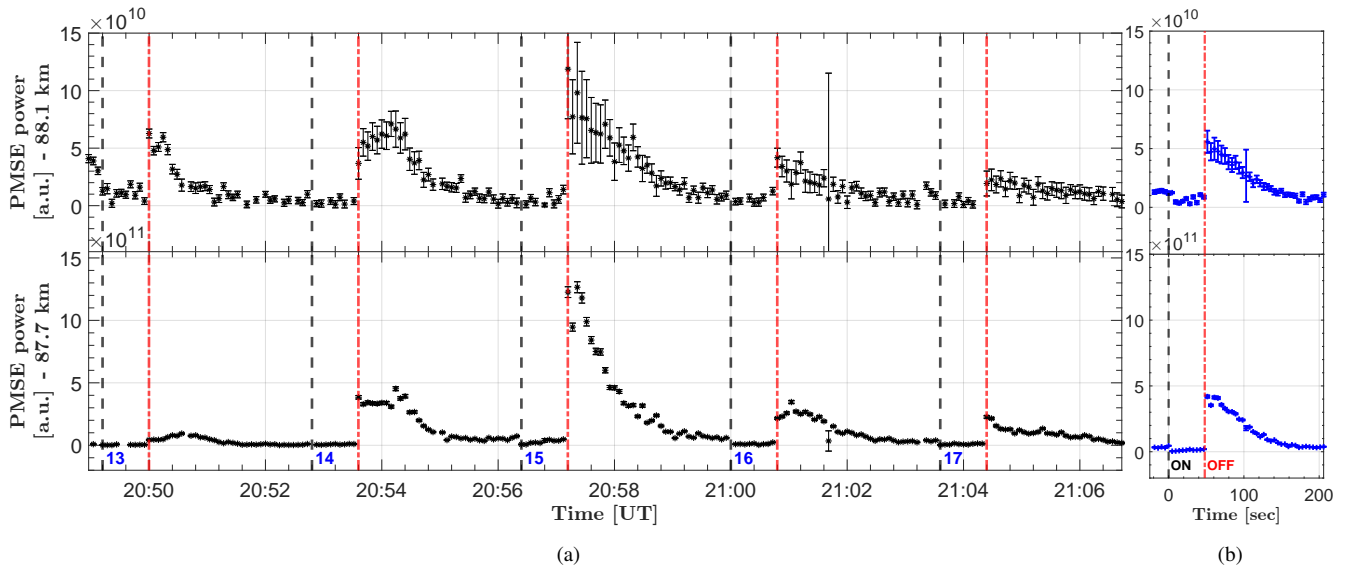
Figure 14. Individual overshoot curves (a) from interval A (from Fig. 13 shown with their corresponding altitude average on the ~~right hand~~ right-hand side (b). Heating cycle numbers are shown at the bottom~~as well as the on~~, and ~~off~~ the on-and-off period for the averaged cycles. Note that the Y-axis scale for altitude 88 km is an order of magnitude smaller than for altitude 87.7 km.

Individual heating cycles from intervals B and C are shown in Fig. 15 ~~a~~ (a) with their corresponding altitude average on the ~~right hand~~ right-hand side in blue (Fig. 15 (b) (Note that here the y-axis scale is the same for all the altitude ranges). They cover heating cycles 21, 22, and 23. ~~For the lower altitudes the~~ The overshoots are present for the lower altitudes but are not as high as in interval A. However, the overshoot does not decline evenly but increases again before reaching the initial signal level~~is~~
410 ~~reached~~. This influence can be ~~clearly seen also~~ seen in the averaged heating curve for altitude 86.7 km, where after about 120 seconds, the power starts to increase again. ~~We think that this is~~ This is either because of the beginning influence of particle precipitation on the ionosphere or variation of the PMSE structure due to the long relaxation time (Havnes et al., 2015). This influence is very strong in the subsequent cycle (cycle 24), where the PMSE power increases during the ~~heater on~~ heater-on period. This type of ionospheric variation can influence the observations to ~~an extent that the~~ the extent that heating effects are
415 less visible. In the same time interval (intervals 21, 22, 23) at the altitude above, the overshoots are small, especially for the first cycle (21), while the PMSE power is ~~also rather~~ relatively low. This is in contrast to the observation made at the higher altitude in interval A where a ~~large~~ significant overshoot is observed at low PMSE power. This might indicate that ~~for these two cases~~ there are different conditions at play ~~.~~ for these two cases. Havnes et al. (2015) has mentioned that higher altitudes of PMSE reside in more turbulent conditions, thus a more significant variation in cloud structure and a longer relaxation time
420 after heater turn-off as a result.

(a) (b)
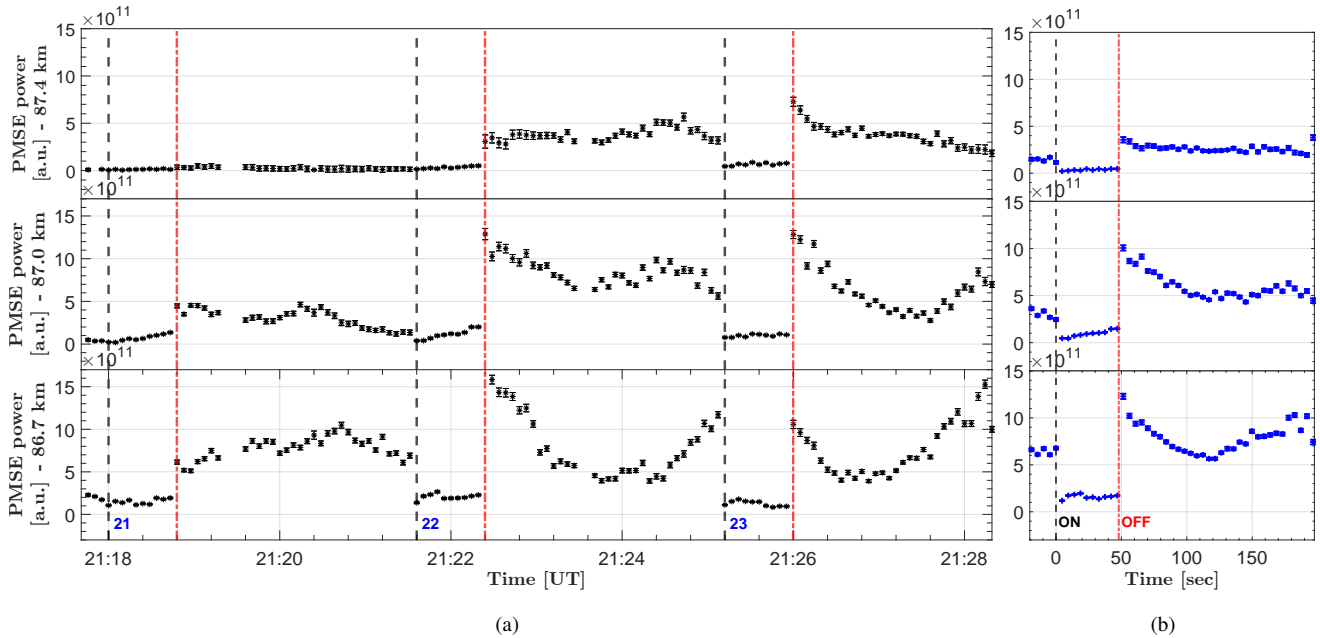
Figure 15. Individual overshoot curves (a) from interval B and C (from Fig. 13) shown with their corresponding altitude average on the ~~right hand~~ right-hand side (b). Heating cycle numbers are shown at the bottom ~~as well as the on~~ and ~~off~~ the on-and-off period for the averaged cycles.

~~Comparison~~ A comparison of the average overshoot curves for each interval (A, B, and C) is shown in ~~Figure 16 on the left side~~ Fig. 16 (a) and their corresponding normalized average curves ~~on the right side~~ in panel (b). The values are normalized to the initial PMSE power taken as the average of the last ~~5~~ five values (24s) before the heater is turned on. This is chosen ~~so that we~~ to have sufficient data when some measurement points are missing and to better compare to the rest of the data used in this article which are at a resolution of 24 seconds. Data were normalized after averaging the cycles from each interval. We can ~~clearly~~ see that the highest normalized overshoot (~~right~~ b) is the one from interval A, which has the lowest background PMSE power (~~left~~ a) and that the lowest normalized overshoot is from interval C ~~that~~, which has the corresponding highest PMSE background power. This high PMSE power is possibly due to an onset of precipitation which becomes apparent in the subsequent cycle 24 right after intervals B and C.

(a)   (b)
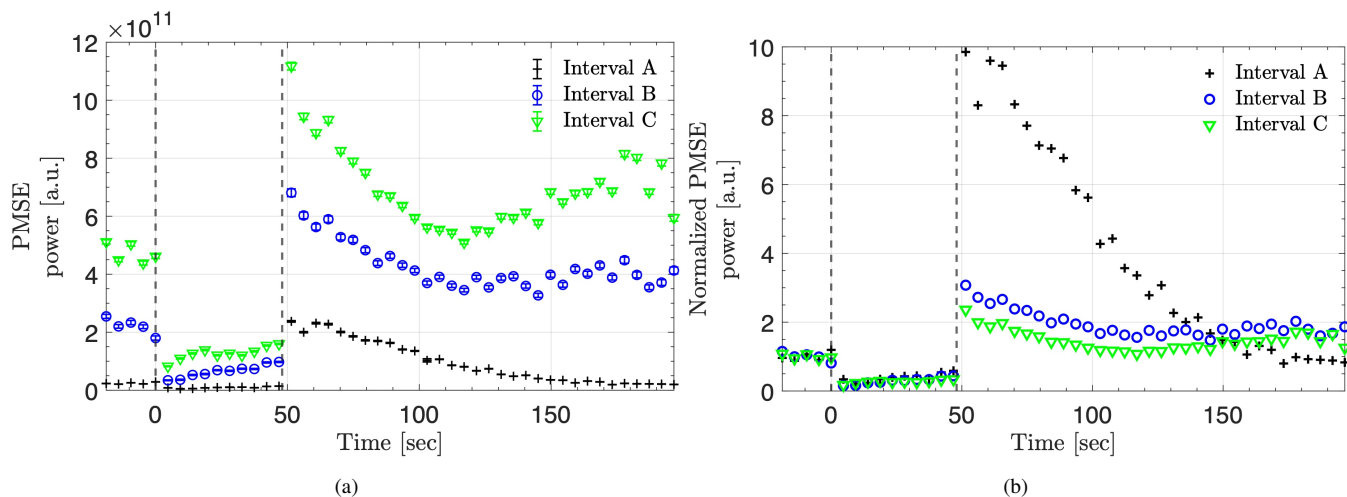
Figure 16. Average overshoot curves for each respective interval (~~right~~left) and normalized average overshoot curves (~~left~~right) for the same intervals. They are normalized with the average of the last ~~5~~ five values before ~~the~~ heater was turned on.

430 We compare these selected overshoot curves to a computational model ~~which was~~ initially developed at Virginia Tech. It treats the plasma as a fluid including an arbitrary number of charged particles, neutral particles, and dust particles; the dust charging is described in the Orbital-Motion-Limited (OML) approach (see, e.g., Scales and Mahmoudian (2016)). The ~~parameters of the model~~model's parameters include the electron diffusion time scale, the charging time scale, and the time evolution of electron and ion densities. The dust charging causes electron density depletion, and the amplitude of electron

435 density fluctuations determines the radar back-scattered amplitude. The simulations assume an initial plasma temperature of $T_i = 150\ K$ and a background electron density of $2 * 10^9\ m^{-3}$. Which fits well with the same parameters derived from the ~~IRI-model~~ IRI model (2016) for the time and date of the observation. The simulation also assumes a reduced photo-emission rate used in the charging equations in line with the experiments being done for conditions with low photo-emission.

   The resulting simulated overshoot curves are shown ~~on the right~~ in Fig. 17 (b) and for comparison are the averaged and

440 normalized observations from intervals A, B, and C (marked in ~~the~~ same color and symbol as previous figures) shown on the left. The simulations ~~show~~ best fit to the observed overshoot curves for 3 nm dust particles. However, there is little difference for similar sizes of dust (e.g., 3-4 nm). This result fits well with the altitude range we measure the observed PMSE echoes since~~in general~~, in general, we can assume to find smaller particles of dust at higher altitudes (however subject to neutral air movement) as well as the fact that there were no NLCs observed and thus the particles were not optically visible (larger >20

445 nm).

   The ~~normalised~~ normalized and averaged data from interval A has a higher overshoot than ~~what~~ the simulations can produce, where the simulation has an overshoot of around 8.4~~while the~~. At the same time, the observations show an overshoot of almost 9.9. ~~Note also the~~ The timescale of the simulation for interval A runs for 300 seconds, while the observation has a much quicker equalization towards the "background" PMSE value/undisturbed plasma values. For the simulation to reach such a

450 high overshoot, the ratio between dust and electron number density is only at 35 %, and with a heating ratio increase for electron temperature of 8 times the pre-heater value. This would indicate that the dust density is lower than for the other two intervals and that the ~~effect of the heating~~ heating effect is consequently larger. As discussed later, The electrons gain a higher temperature, and charging onto the dust particles is ~~consequently more effective. Where~~, therefore, more effective, where some dust particles can gain more than a single charge ~~as is discussed later~~.

455 ~~Comparison~~ A comparison of observations for intervals B and C and their corresponding simulations show a better ~~"match"~~ agreement where the overshoot and relaxation are very similar. For these overshoots to be produced in the simulation, the ratio of dust to electrons ~~is higher~~must be higher, with 60 % for interval B and 68 % for interval C. The increase at the end of the relaxation period for both intervals is not reproduced in the simulations~~,~~; this is assumed to be due to the influence of the precipitation that occurs clearly in cycle 24 and ~~already is~~ is already increasing the background PMSE power in the

460 previous cycles. Compared to the observations, the simulated signals drop ~~more slowly~~ slower during the heater ON phase and rise more slowly to the overshoot when the heater is switched off again. The measured response of the PMSE to the heating is instantaneous within the 4.8 seconds resolution of the data. A possible explanation for this difference is that the numerical model might have missing parameters or processes ~~that are present in order~~ to simulate this increase. This is in contrast to the decrease we see in most ~~of the observations~~observations, as was discussed previously.

(a)   (b)
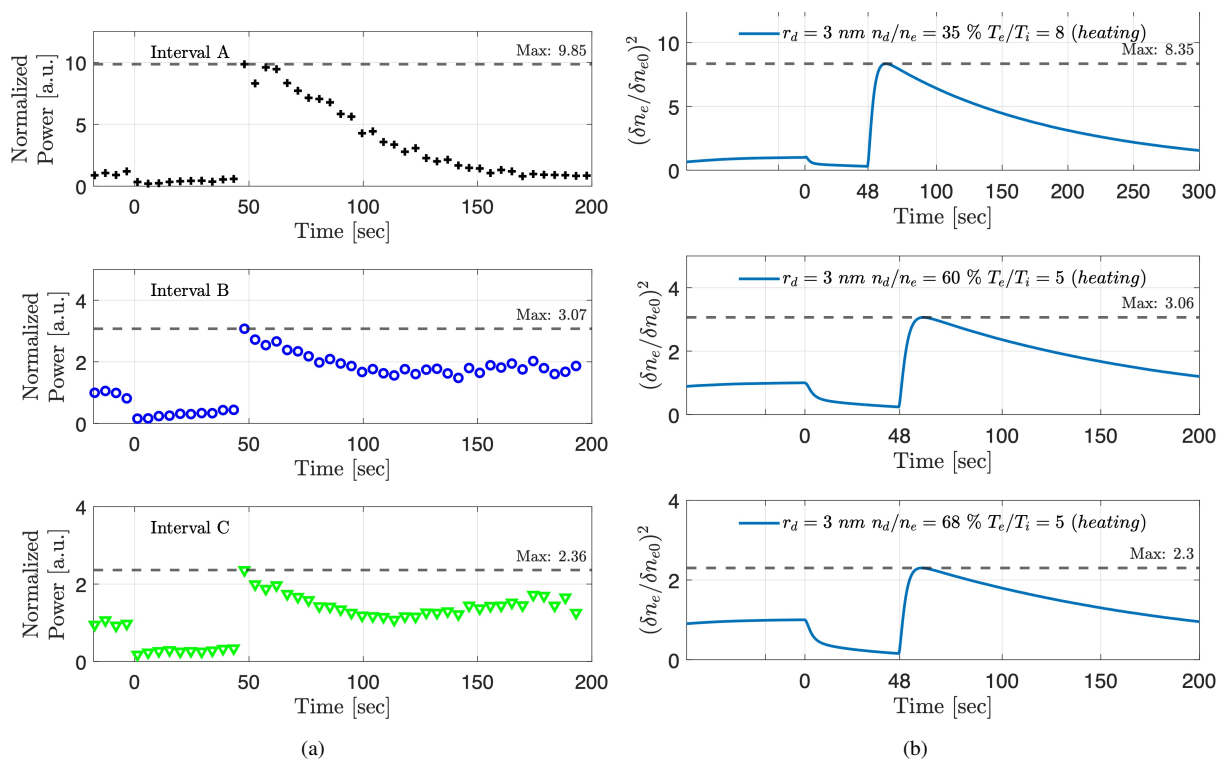
Figure 17. Comparison of the averaged and normalized heating cycles for each interval (left) to its corresponding simulation of the overshoot cycles (right). Note the longer timescale of simulation of interval A (longer time needed for simulation to return to equilibrium)

On the left-hand side in Fig. 18 (a), we can see the average charge number found for the simulation for each respective interval (marked in the figure). For interval A the average charge number reaches a maximum of about 1.38 charges per dust particle during the heater on phase. This indicates that to achieve such a high overshoot, the charging efficiency of the dust particles needs to be high and that (due to high electron heating temperature) many dust particles will gain more than one negative charge during the heating cycle. Note the longer timescale shown in the simulation for interval A (300 seconds), indicating that it takes longer for the overall average charge on the dust particles to equalize back to pre-heater values. As was mentioned before, the dust population is much lower for interval A compared to the other two intervals since the ratio of dust to electrons is lower. Consequently, the significant increase in temperature (by a factor of 8) causes a larger average charge number on the dust particles during the heater on phase. For the other intervals (B and C), the maximum average charge number is less than one during the on phase of the heater for both cases, with interval B being around 0.9 charges per dust. For interval C, the average dust charge lies at about 0.86. This corresponds well with the observed and simulated overshoot curves from Fig. 17, where the higher overshoot is observed in interval B. Thus the average charge number is consequently higher. So the effective charging of the dust during heater on for these intervals is less than for interval A, and a smaller overshoot is observed.

On the right-hand side in Fig. 18 (b), we have the ratio of the diffusion time to the charging time scales for each respective interval. Here we can see the variation between the two timescales and how this changes during the heating cycle. For all the intervals, there is an increase in the ratio when the heater turns on, a relaxation during the heater on period, a sharp increase when the heater is turned off, and a slow decrease during the heater off period. The significant increase in the heater-on time could be understood as the charging timescale becoming smaller with increased electrons charging onto dust particles due to the increased electron temperature. This corresponds well with the increased average electron charge on the dust particles seen in Fig. 18 (a). Here the average dust charge is highest for interval A, and the ratio of timescales is also highest for this interval, which might indicate a faster charging timescale for that interval than for the other two. The increase at heater turn-off is also due to a decrease in the charging times; more dust is being charged now by the ion portion of the plasma, which drags the electrons along and causes the observed overshoot. Thus for interval A the simulation of the overshoot curve fits best with a lower ratio of dust particles to electron density. Therefore we might argue that there is more plasma than in the other two intervals. This larger plasma population might then charge the dust more quickly, causing a smaller charging timescale and, consequently, a larger overshoot in interval A.
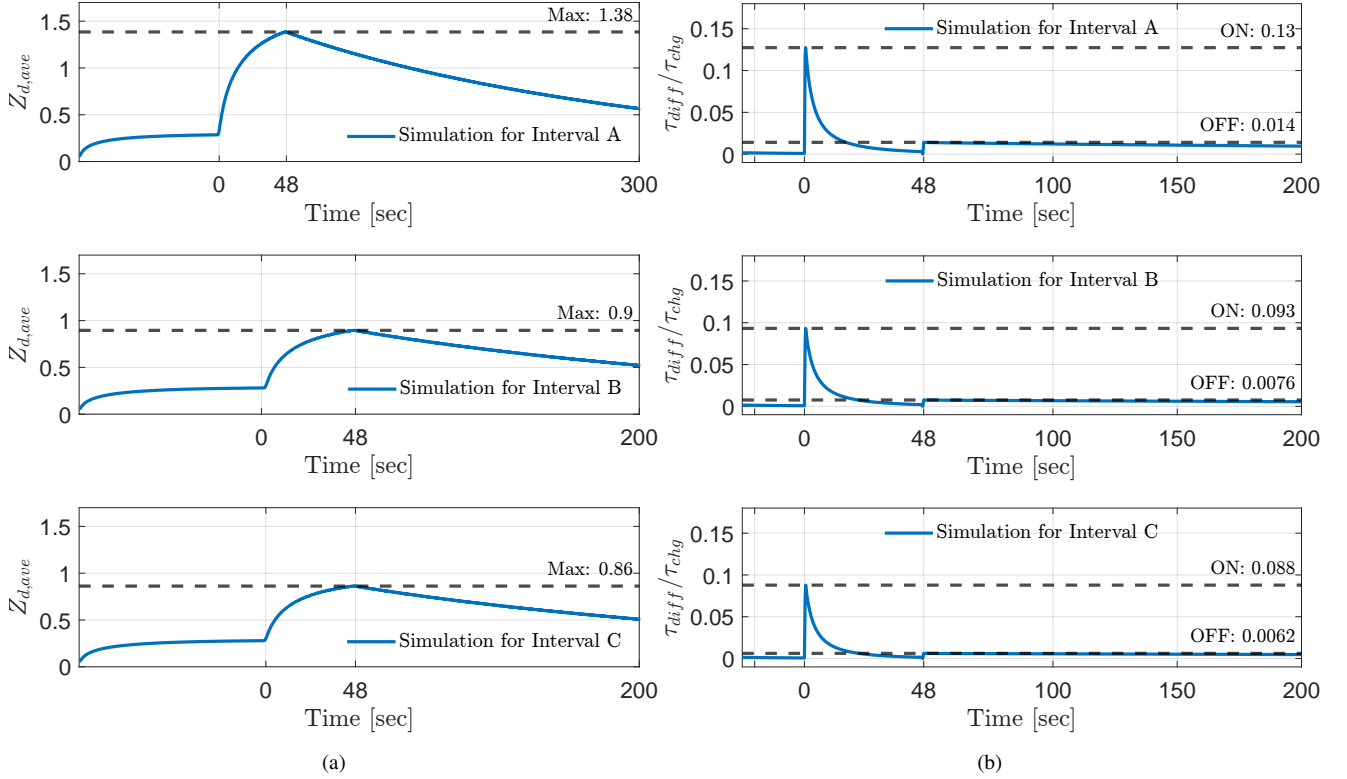
Figure 18. Simulations of average dust charge number on the left (a) for each respective interval and the ratio between the diffusion time and the charging time scales for ~~the~~ same intervals on the right (b).

Another ~~influence also worth noting is the possible difference~~ difference could arise in the diffusion timescales ~~of~~ in the respective intervals~~before the heater is turned off. This difference could arise due to the higher altitude of interval A and consequently a~~ . The diffusion timescale is proportional to the ion-neutral collision frequency, which decreases with decreasing neutral density. Hence in interval A at a higher altitude and with lower neutral density. ~~This small reduction in neutral density causes a smaller ion-neutral collision frequency, and consequently a smaller diffusion time scale due to the diffusion being proportional to the collision frequency. Where the diffusion~~ , the diffusion timescale can be ~~estimated with the following equation (Chen and Scales, 2005):~~

$$\tau_{dff} \approx \nu_{in} \left(\frac{\lambda_{irreg}}{2\pi v_{th}} \right)^2 \frac{1}{(1 + \frac{T_e}{T_i})(1 + \frac{z_d n_{d0}}{n_{e0}})}$$

~~Where ν_{in} is the~~ shorter than in the other interval (Havnes et al., 2015). The estimated ion-neutral ~~collision frequency, λ_{irreg} is the wavelength of the irregularity and is given by $2 * \lambda_R$ (the radar wavelength), v_{th} is the mean ion thermal velocity, T_e and T_i are the electron and ion temperatures respectively. The dust charge number is given by Z_d, n_d is the dust number density and~~

n_e is the background electron number density. The ion-neutral collision frequency ν_{in} (polarization) can be estimated using the following equation ((Ieda, 2020; Cho et al., 1998) see ref. for relevant constants used in the equation):

$$\nu_{in} = 25.879 \times 10^{-16} \frac{N_n}{\sqrt{m_i}} \sum_t F_t \sqrt{\frac{m_n \alpha_0}{m_i + m_n}}$$

Where N_n is the neutral density (in m^{-3}), α_0 is the neutral gas polarizability (10^{-24} cm^3), m_i and m_n are the ion and neutral mass (in atomic mass units - amu) respectively. The sum can be summed over the fractional volume of the neutral gas present, F_t, of each respective neutral constituent (here used most abundant; molecular nitrogen, oxygen and atomic argon). A quick estimate of the diffusion timescale right before the heater is turned on and right before it is turned off using values for the neutral density (frequencies are given in Table 3, which are derived using neutral density from NRLMSISE-00 Atmosphere Model (Hedin, 1991)) is shown in Table 3 below. Here we can see that the estimated timescale of the diffusion for interval A is lower than for the other two intervals for both diffusion estimates, indicating that a smaller charging timescale is needed to get the timescale ratio shown in Fig. 18b an thus a much more effective charging must be present for interval A.

Table 3. Neutral density for each interval from NRLMSISE-00 Atmosphere Model)(Hedin, 1991) taken at 21 UT and the estimated ion-neutral collision frequency (Eqsee. ??) and a rough estimate of the diffusion timescale (Eq. ?? right before heater is turned on and right before the heater is turned off(Ieda, 2020; Cho et al., 1998)

Interval	Neutral density $[m^{-3}]$	v_{in} [1/s]	τ_{dff} at 0 sec τ_{dff} at 48 sec
A	$1.19 * 10^{20}$	$3.44 * 10^4$	0.0256 0.0188
B	$1.33 * 10^{20}$	$3.85 * 10^4$	0.0407 0.0304
C	$1.48 * 10^{20}$	$4.26 * 10^4$	0.0443 0.0327

The timescale that is the fastest is the dominating one. So when the heater turns on, the diffusion timescale might be lower for interval A. So when the heater is turned on, the diffusion timescale decreases even more due to its dependence on the temperature ratio (Te/Ti), and we expect/need a larger more significant temperature increase for the electrons in interval A to explain such a large overshoot. As the heater is turned on, the charging timescale decreases due to the increase in electron temperatureand a . A larger charging effect is seen in the interval A simulation (average charge number) compared to the other intervalsand consequently . Consequently, a larger overshoot is seen.

So to summarizeit might appear that , the decreased diffusion timescale for interval A due to decreased reduced neutral density and the large significant increase in electron temperature combined could help explain the large overshoot that is seen for interval A. However where the effect of the heater The higher electron temperature could be explained by greater absorption of the heater's energy in the interval. According to Havnes et al. (2015), the amount of electron density per altitude will determine where the heater's energy is absorbed and how muchmust have something to say. If some amount of the heater

effect is absorbed below the PMSE layer due to increased ionization it could influence the observed overshoot. And same for layers that absorb much of the incoming heater radio wave could cause a larger overshoot. This generally causes lower altitudes of PMSE to become more heated than higher altitudes. Interval A is at a higher altitude than the other two intervals. Still, the precipitation present in cycle 18 before intervals B and C could cause the altitude regions below these intervals to have a higher electron content and, thus more absorption of the heater's energy below.

5 Discussion and Conclusion

For the presented observations, we find that the artificial heating affects the PMSE signals during less than half of all the observed heating cycles with a pre-heated PMSE power $R_0 > 10^{10.5}$; the average reduction of the power is about 25 % from the pre-heated value. The cutoff, $R_0 > 10^{10.5}$, excludes cycles that do not show PMSE and cycles being highly influenced by noise. With this criterion, we covered most of the PMSE. However, some very faint ones were excluded, and some were affected by heating and showed large overshoots. We find that the heating has little effect on PMSE during ionospheric conditions with particle precipitation which other authors also see. This is especially so for strong and moderate particle precipitation. We assume that under these conditions of higher ionization, the heating waves are mainly absorbed in lower altitudes, thus not causing a heating effect in the PMSE layer. Often the background ionospheric conditions strongly influence the PMSE profile during one heater cycle and it is thus challenging to derive a correct relaxation time, which would be an interesting parameter because it depends on the dust conditions present in the layer.

As to the shape of the PMSE modulation curves, the variation of the PMSE during the heater-on period(from R_1 to R_2) is affected by two competing processes: the charging and the diffusion. For the presented observations, most heating cycles display a signal decrease from R1 to R2. Less than half of the cycles influenced by heating show an overshoot when the heater is turned off. However, observed overshoots are generally high and, in some cases, very high. These high overshoots could be attributed to the dust charge in the presented observations being more strongly influenced by heating, as the influence of photoemission is smaller than during daytime observations.

It is also possible that the size of ice particles and their formation and sublimation rates are different toward the end of the PMSE season; most other heating studies were carried out earlier in the year. A general trend towards a more extended PMSE season (Latteck et al., 2021) and larger particles at PMSE altitudes (at high latitudes) due to increased water vapor content (Lübken et al., 2021) could also cause these recent PMSE observations to show different modulation curves.

The computational overshoot model we considered cannot account for some of the high overshoot cases we observed, and we are unaware of a model that does so. Some processes might need to be included to reproduce these cases of large overshoots. The influence of variation in the

ionospheric background with time over the cycles reduces the overshoots and dominates the relaxation phase. We form~~however~~ , however, averaged curves as was done in other studies and compare those to the model calculations. We find that simulations ~~assuming~~ with dust size around 3 nm ~~fits best~~ best fit to all cases considered ~~; while~~ .

While different electron heating ratios and ~~different ratios of dust to electron density~~ dust-to-electron densities are needed to match the observational data, ~~with a larger~~ a larger temperature heating ratio and a lower dust density ~~is needed~~ are required to best match the large average overshoot ~~seen.~~

~~Finally, the heating itself is an unknown. Since the electron temperature influences the charging processes observed in the heating cycles it is important to correctly estimate the electron temperature during the heating. Recently, Myrvang et al. (2021) showed that the presence of dust particles affects the HF heating and the resulting electron temperature as a function of altitude. This implies that when estimating the electron temperature, one needs to make assumptions on the dust components~~ observed. The amount of absorption from the heater's energy is important in how effectively the electrons can be heated. And since there is precipitation between the first interval with large overshoots and the two other intervals, it stands to reason that the altitudes below the PMSE ~~. In addition the electron density below the PMSE plays a role. This might be the reason why we see large overshoots for example in the high altitude layer of Area 2 from 15 of August 2018 where there is no precipitation before the layer starts and the PMSE power is relatively low. Thus the heating might be quite effective in this case than for the later conditions where precipitation causes an overall higher electron density and therefore also~~ layer have increased electron content after moderate precipitation. This causes a larger absorption of the heater~~waves already~~ 's energy below the PMSE ~~.~~ layer. Therefore a combination of decreased heater energy and lower diffusion time can help explain the large overshoot in the first interval.

~~The~~ We conclude that the presented observations during HF heating confirm that ~~PMSE amplitudes are modulated by~~ high-power radio waves modulate PMSE amplitudes, with the observed modulation varying on short spatial and temporal scales. ~~Presented~~ The presented observations differ from previous studies since they are done late in the PMSE season ~~as well as~~ and during lower solar illumination (dusk/night). In general, we see both an influence of the ~~heater as well as~~ heating and an overshoot in about half of the heating cycles, which is somewhat lower than previous observations done earlier in the season around midday. We see ~~cases of~~ very high overshoots compared to ~~other previous observations . However, due to the large background and ionospheric variability, any specific determination of dust parameters or conditions causing these large overshoots is difficult as there are many unknown parameters related to PMSE heating. These include formation and disappearance of ice particles, horizontal and vertical movement of the layer, active turbulence, dust charge and size distributions within the PMSE layer and in the layer where the effect of the heater is mainly absorbed.~~ previous observations and note that increased PMSE power is connected to smaller overshoots.

Code and data availability. EISCAT VHF data used is available under https://madrigal.eiscat.se/madrigal. EISCAT GUISDAP analysis tool used is available under https://eiscat.se/scientist/user-documentation/guisdap/. Information on the Manda radar code is available under https:

//eiscat.se/wp-content/uploads/2021/03/Experiments_v20210302.pd. Code and plots used in this article can be accessed at the UIT data repository; https://doi.org/10.18710/NGISOA

595 *Author contributions.* TG, AP and IM did the data analysis and interpretation. Planning of the observations was done by IM, MR, IH and PD. Temperature data from AURA satellite provided by PD. Investigation of overshoot done by TG and AM and simulations and model provided by AM. Everybody participated in manuscript writing, preparation and interpretation.

Competing interests. The authors declare that they have no conflict of interest. At least one of the (co-)authors is a member of the editorial board of Annales Geophysicae.

600 *Acknowledgements.* This work is carried out within a project funded by the Research Council of Norway, NFR 275503. The Norwegian EISCAT participation is funded by The Research Council of Norway project 245683. The publication charges for this article have been funded by a grant from the publication fund of UiT The Arctic University of Norway. The EISCAT International Association is supported by research organizations in Norway (NFR), Sweden (VR), Finland (SA), Japan (NIPR), China (CRIRP), and the United Kingdom (NERC).

References

Belova, E., Smirnova, M., Rietveld, M., Isham, B., Kirkwood, S., and Sergienko, T.: First observation of the overshoot effect for polar mesosphere winter echoes during radiowave electron temperature modulation, Geophysical research letters, 35, 2008.

Biebricher, A., Havnes, O., Hartquist, T., and LaHoz, C.: On the influence of plasma absorption by dust on the PMSE overshoot effect, Advances in Space Research, 38, 2541–2550, 2006.

Chen, C. and Scales, W.: Electron temperature enhancement effects on plasma irregularities associated with charged dust in the Earth's mesosphere, Journal of Geophysical Research: Space Physics, 110, 2005.

Chilson, P. B., Belova, E., Rietveld, M. T., Kirkwood, S., and Hoppe, U.-P.: First artificially induced modulation of PMSE using the EISCAT heating facility, Geophysical research letters, 27, 3801–3804, 2000.

Cho, J. Y. and Röttger, J.: An updated review of polar mesosphere summer echoes: Observation, theory, and their relationship to noctilucent clouds and subvisible aerosols, Journal of Geophysical Research: Atmospheres, 102, 2001–2020, 1997.

Cho, J. Y., Sulzer, M. P., and Kelley, M. C.: Meteoric dust effects on D-region incoherent scatter radar spectra, Journal of atmospheric and solar-terrestrial physics, 60, 349–357, 1998.

Czechowsky, P., Rüster, R., and Schmidt, G.: Variations of mesospheric structures in different seasons, Geophysical Research Letters, 6, 459–462, 1979.

Dalin, P., Kirkwood, S., Moström, A., Stebel, K., Hoffmann, P., and Singer, W.: A case study of gravity waves in noctilucent clouds, in: Annales Geophysicae, vol. 22, pp. 1875–1884, Copernicus GmbH, 2004.

Ecklund, W. and Balsley, B.: Long-term observations of the Arctic mesosphere with the MST radar at Poker Flat, Alaska, Journal of Geophysical Research: Space Physics, 86, 7775–7780, 1981.

Giono, G., Strelnikov, B., Asmus, H., Staszak, T., Ivchenko, N., and Lübken, F.-J.: Photocurrent modelling and experimental confirmation for meteoric smoke particle detectors on board atmospheric sounding rockets, Atmospheric Measurement Techniques, 11, 5299–5314, 2018.

Havnes, O.: Polar Mesospheric Summer Echoes (PMSE) overshoot effect due to cycling of artificial electron heating, Journal of Geophysical Research: Space Physics, 109, 2004.

Havnes, O., La Hoz, C., Rietveld, M. T., Kassa, M., Baroni, G., and Biebricher, A.: Dust charging and density conditions deduced from observations of PMWE modulated by artificial electron heating, Journal of Geophysical Research: Atmospheres, 116, 2011.

Havnes, O., Pinedo, H., La Hoz, C., Senior, A., Hartquist, T. W., Rietveld, M. T., and Kosch, M. J.: A comparison of overshoot modelling with observations of polar mesospheric summer echoes at radar frequencies of 56 and 224 MHz, Annales Geophysicae, 33, 737–747, https://doi.org/10.5194/angeo-33-737-2015, https://angeo.copernicus.org/articles/33/737/2015/, 2015.

Hedin, A. E.: Extension of the MSIS thermosphere model into the middle and lower atmosphere, Journal of Geophysical Research: Space Physics, 96, 1159–1172, 1991.

Hervig, M. E., Deaver, L. E., Bardeen, C. G., Russell III, J. M., Bailey, S. M., and Gordley, L. L.: The content and composition of meteoric smoke in mesospheric ice particles from SOFIE observations, Journal of Atmospheric and Solar-Terrestrial Physics, 84, 1–6, 2012.

Hunten, D. M., Turco, R. P., and Toon, O. B.: Smoke and dust particles of meteoric origin in the mesosphere and stratosphere, Journal of Atmospheric Sciences, 37, 1342–1357, 1980.

Ieda, A.: Ion-neutral collision frequencies for calculating ionospheric conductivity, Journal of Geophysical Research: Space Physics, 125, e2019JA027 128, 2020.

Ignat'ev, Y. A.: Influence of heating of the ionosphere by high-power radio emission on the sporadic E layer, Radiophysics and Quantum Electronics, 18, 1010–1013, 1975.

Kassa, M., Havnes, O., and Belova, E.: The effect of electron bite-outs on artificial electron heating and the PMSE overshoot, 2005.

Kavanagh, A., Honary, F., Rietveld, M., and Senior, A.: First observations of the artificial modulation of polar mesospheric winter echoes, Geophysical research letters, 33, 2006.

Latteck, R., Renkwitz, T., and Chau, J. L.: Two decades of long-term observations of polar mesospheric echoes at 69° N, Journal of Atmospheric and Solar-Terrestrial Physics, 216, 105 576, 2021.

Lehtinen, M. S. and Huuskonen, A.: General incoherent scatter analysis and GUISDAP, Journal of Atmospheric and Terrestrial Physics, 58, 435–452, 1996.

Lübken, F.-J.: Thermal structure of the Arctic summer mesosphere, Journal of Geophysical Research: Atmospheres, 104, 9135–9149, 1999.

Lübken, F.-J., Baumgarten, G., and Berger, U.: Long term trends of mesopheric ice layers: A model study, Journal of Atmospheric and Solar-Terrestrial Physics, 214, 105 378, 2021.

Mahmoudian, A., Scales, W. A., Kosch, M., Senior, A., and Rietveld, M.: Dusty space plasma diagnosis using temporal behavior of polar mesospheric summer echoes during active modification, in: Annales Geophysicae, vol. 29, pp. 2169–2179, Copernicus GmbH, 2011.

Mahmoudian, A., Senior, A., Scales, W., Kosch, M. J., and Rietveld, M.: Dusty space plasma diagnosis using the behavior of polar mesospheric summer echoes during electron precipitation events, Journal of Geophysical Research: Space Physics, 123, 7697–7709, 2018.

Mahmoudian, A., Kosch, M. J., Vierinen, J., and Rietveld, M. T.: A new technique for investigating dust charging in the PMSE source region, Geophysical Research Letters, 47, e2020GL089 639, 2020.

Mann, I., Häggström, I., Tjulin, A., Rostami, S., Anyairo, C., and Dalin, P.: First wind shear observation in PMSE with the tristatic EISCAT VHF radar, Journal of Geophysical Research: Space Physics, 121, 11–271, 2016.

Megner, L., Rapp, M., and Gumbel, J.: Distribution of meteoric smoke–sensitivity to microphysical properties and atmospheric conditions, Atmospheric Chemistry and Physics, 6, 4415–4426, 2006.

Myrvang, M., Baumann, C., and Mann, I.: Modelling of the influence of meteoric smoke particles on artificial heating in the D-region, Annales Geophysicae Discussions, pp. 1–21, 2021.

Pinedo, H., La Hoz, C., Havnes, O., and Rietveld, M.: Electron–ion temperature ratio estimations in the summer polar mesosphere when subject to HF radio wave heating, Journal of Atmospheric and Solar-Terrestrial Physics, 118, 106–112, https://doi.org/https://doi.org/10.1016/j.jastp.2013.12.016, https://www.sciencedirect.com/science/article/pii/S1364682613003349, recent progress from networked studies based around MST radar, 2014.

Rapp, M. and Lübken, F.-J.: Electron temperature control of PMSE, Geophysical research letters, 27, 3285–3288, 2000.

Rapp, M. and Lübken, F.-J.: Polar mesosphere summer echoes (PMSE): Review of observations and current understanding, 2004.

Rapp, M. and Thomas, G. E.: Modeling the microphysics of mesospheric ice particles: Assessment of current capabilities and basic sensitivities, Journal of Atmospheric and Solar-Terrestrial Physics, 68, 715–744, 2006.

Rietveld, M., Kohl, H., Kopka, H., and Stubbe, P.: Introduction to ionospheric heating at Tromsø—I. Experimental overview, Journal of atmospheric and terrestrial physics, 55, 577–599, 1993.

Rietveld, M. T., Senior, A., Markkanen, J., and Westman, A.: New capabilities of the upgraded EISCAT high-power HF facility, Radio Science, 51, 1533–1546, 2016.

Rosinski, J. and Snow, R.: Secondary particulate matter from meteor vapors, Journal of Atmospheric Sciences, 18, 736–745, 1961.

Scales, W. and Mahmoudian, A.: Charged dust phenomena in the near-Earth space environment, Reports on Progress in Physics, 79, 106 802, 2016.

680 Strelnikova, I. and Rapp, M.: Majority of PMSE spectral widths at UHF and VHF are compatible with a single scattering mechanism, Journal of atmospheric and solar-terrestrial physics, 73, 2142–2152, 2011.

Tanaka, K. K., Mann, I., and Kimura, Y.: Formation of ice particles through nucleation in the mesosphere, Atmospheric Chemistry and Physics Discussions, 2021, 1–17, https://doi.org/10.5194/acp-2021-728, https://acp.copernicus.org/preprints/acp-2021-728/, 2021.

Tjulin, A.: EISCAT experiments, EISCAT Scientific Association,(March), 2017.

685 Ullah, S., Li, H., Rauf, A., Meng, L., Wang, B., and Wang, M.: Statistical study of PMSE response to HF heating in two altitude regions, Earth, Planets and Space, 71, 1–14, 2019.

Additional figures depicting the observations

Additional figures are given in Appendix A, with selected cases discussed in more detail in Appendix ??. Appendix ?? then contains the supplementary material to the paper. They show each marked area in the observations, a comparison of the power

690 amplitudes for each respective measurement range and Appendix ?? contains , and histograms of these amplitudes. All figures can also be accessed at the UIT data repository; https://doi.org/10.18710/NGISOA.

Appendix A: Overview of the measurements

Table A1. Days of measurements and selected areas. t_start and t_end define the beginning and the end of the area. The altitude of the atmosphere, where the analysis is done, are described with h_low and h_high.

Day / Area	t_start	t_end	h_low	h_high
Night of Aug 11/12, 2018	Aug 11, 20:00	Aug 12, 02:00	80.0 km	110.0 km
Area 1	Aug 11, 21:36	Aug 11, 22:42	83.4 km	85.6 km
Area 2	Aug 11, 23:06	Aug 12, 01:17	86.3 km	90.0 km
Area 3	Aug 12, 00:00	Aug 12, 01:28	83.4 km	86.4 km
Night of Aug 15/16, 2018	Aug 15, 20:00	Aug 16, 02:00	80.0 km	110.0 km
Area 1	Aug 15, 20:06	Aug 15, 20:25	88.1 km	89.6 km
Area 2	Aug 15, 20:48	Aug 15, 21:47	86.3 km	88.5 km
Area 3	Aug 15, 21:57	Aug 15, 22:59	83.4 km	87.8 km
Night of Aug 05/06, 2020	Aug 05, 20:25	Aug 06, 00:00	80.0 km	110.0 km
Area 1	Aug 05, 21:25	Aug 11, 22:50	82.0 km	88.0 km
Area 2	Aug 05, 22:50	Aug 12, 23:50	83.0 km	87.0 km
Area 3	Aug 05, 22:45	Aug 06, 00:00	90.0 km	100.0 km
Night of Aug 06/07, 2020	Aug 06, 21:15	Aug 07, 02:00	80.0 km	110.0 km
Area 1	Aug 06, 22:53	Aug 07, 02:00	81.5 km	88.0 km
Area 2	Aug 06, 22:43	Aug 06, 23:29	91.0 km	94.0 km
Area 3	Aug 06, 21:15	Aug 06, 22:15	82.0 km	85.0 km

Table A2. Values of ERP given in the EISCAT Heating facility logs from sample beam patterns for each of the measurements for reference. It seems that on 6 Aug 2020 at around 23:08:25 UT three transmitters changed phases such that the beam became broader, with about 360 MW X-mode and 17 MW O-mode which remained so until the end, which is why we have 359 MW X-mode at 01:07:13 UT (7 of August) below) 359 at 7

Day	Time (UT)	ERP
11 August 2018	20:50:13	560 MW
12 August 2018	01:20:13	541 MW
15 August 2018	20:06:19	568 MW
16 August 2018	00:39:49	580 MW
05 August 2020	20:47:01	495 MW
06 August 2020	19:29:58	567 MW
7 August 2020	01:07:13	359 MW

A1 ~~Night of Aug 11/12, 2018~~

~~Back scattered power as function of altitude and heating intervals observed during the night of August 11/12, 2018 in Area 1.~~
695 ~~Back scattered power as function of altitude and heating intervals observed during the night of August 11/12, 2018 in Area 2.~~
~~Back scattered power as function of altitude and heating intervals observed during the night of August 11/12, 2018 in Area 3.~~

A1 ~~Night of Aug 15/16, 2018~~

700 ~~Back scattered power as function of altitude and heating intervals observed during the night of August 15/16, 2018 in Area 1.~~
~~Back scattered power as function of altitude and heating intervals observed during the night of August 15/16, 2018 in Area 2.~~
~~Back scattered power as function of altitude and heating intervals observed during the night of August 15/16, 2018 in Area 3.~~

705 ## A1 ~~Night of Aug 05/06, 2020~~

~~Back scattered power as function of altitude and heating intervals observed during the night of August 05/06, 2020 in Area 1.~~
~~Back scattered power as function of altitude and heating intervals observed during the night of August 05/06, 2020 in Area 2.~~

Back scattered power as function of altitude and heating intervals observed during the night of August 05/06, 2020 in Area 3. It should be noted that other limits of the colour scale have been chosen for this plot.

A1   Night of Aug 06/07, 2020

Back scattered power as function of altitude and heating intervals observed during the night of August 06/07, 2020 in Area 1.
Back scattered power as function of altitude and heating intervals observed during the night of August 06/07, 2020 in Area 2. It should be noted that other limits of the colour scale have been chosen for this plot.
Back scattered power as function of altitude and heating intervals observed during the night of August 06/07, 2020 in Area 3.

Appendix B: Selected detailed PMSE signal

A1   Night of Aug 15/16, 2018

Back scattered power at altitude 88.8 km and heating intervals observed during the night of . The colour of the dots follow the colour scale of figure **??**.
Back scattered power at altitude 87.4 and 87.8 km and heating intervals observed during the night of . The colour of the dots follow the colour scale of figure **??**.
Back scattered power at altitude 87.4 and 87.8 km and heating intervals observed during the night of . Each 4.8 seconds there is a data point, usually the interval is 24 seconds. The colour of the dots follow the colour scale of figure **??**.

A1   Night of Aug 05/06, 2020

Back scattered power at altitude 85.2 and 85.6 km and heating intervals observed during the night of . The colour of the dots follow the colour scale of figure **??**.

Appendix B: Comparison of the power amplitudes

Comparison of the power amplitudes observed on the 11 August 2018 in Area 1.
Comparison of the power amplitudes observed on the 11 August 2018 in Area 2.
Comparison of the power amplitudes observed on the 11 August 2018 in Area 3.
Comparison of the power amplitudes observed on the 15 August 2018 in Area 1.
Comparison of the power amplitudes observed on the 15 August 2018 in Area 3.
Comparison of the power amplitudes observed on the 5 August 2020 in Area 1.
Comparison of the power amplitudes observed on the 5 August 2020 in Area 3.
Comparison of the power amplitudes observed on the 6 August 2020 in Area 1.

Comparison of the power amplitudes observed on the 6 August 2020 in Area 2.

Comparison of the power amplitudes observed on the 6 August 2020 in Area 3.

Appendix B: Histograms of heating cycle ratios with averages

740   Average of the decline for the observed data on the 11 and 15 August 2018. Only overshoot curves with a minimal background amplitude of $R_0 > 10^{10.5}$ are considered. The ratios are chosen in such a way, that, if we observe an overshoot curve like shown in Figure 1, all ratios are smaller than 1. Thus, the histograms are clipped at a maximum ratio of 3. The green line and the corresponding number displays the mean for all ratios smaller than 1. Average of the decline for the observed data on the 5 and 6 August 2020. Only overshoot curves with a minimal background amplitude of $R_0 > 10^{10.5}$ are considered. The ratios

745 are chosen in such a way, that, if we observe an overshoot curve like shown in Figure 1, all ratios are smaller than 1. Thus, the histograms are clipped at a maximum ratio of 3. The green line and the corresponding number displays the mean for all ratios smaller than 1.

  Average of the overshoot for the observed data on the 11 and 15 August 2018. Only overshoot curves with a minimal background amplitude of $R_0 > 10^{10.5}$ are considered. The ratios are chosen in such a way, that, if we observe an overshoot

750 curve like shown in Figure 1, all ratios are smaller than 1. Thus, the histograms are clipped at a maximum ratio of 3. The green line and the corresponding number displays the mean for all ratios smaller than 1. Average of the overshoot for the observed data on the 5 and 6 August 2020. Only overshoot curves with a minimal background amplitude of $R_0 > 10^{10.5}$ are considered. The ratios are chosen in such a way, that, if we observe an overshoot curve like shown in Figure 1, all ratios are smaller than 1. Thus, the histograms are clipped at a maximum ratio of 3. The green line and the corresponding number displays the mean for

755 all ratios smaller than 1.

  Average of the heating for the observed data on the 11 and 15 August 2018. Only overshoot curves with a minimal background amplitude of $R_0 > 10^{10.5}$ are considered. The ratios are chosen in such a way, that, if we observe an overshoot curve like shown in Figure 1, all ratios are smaller than 1. Thus, the histograms are clipped at a maximum ratio of 3. The green line and the corresponding number displays the mean for all ratios smaller than 1. Average of the heating for the observed data

760 on the 5 and 6 August 2020. Only overshoot curves with a minimal background amplitude of $R_0 > 10^{10.5}$ are considered. The ratios are chosen in such a way, that, if we observe an overshoot curve like shown in Figure 1, all ratios are smaller than 1. Thus, the histograms are clipped at a maximum ratio of 3. The green line and the corresponding number displays the mean for all ratios smaller than 1.

  Average of the recovery for the observed data on the 11 and 15 August 2018. Only overshoot curves with a minimal

765 background amplitude of $R_0 > 10^{10.5}$ are considered. The ratios are chosen in such a way, that, if we observe an overshoot curve like shown in Figure 1, all ratios are smaller than 1. Thus, the histograms are clipped at a maximum ratio of 3. The green line and the corresponding number displays the mean for all ratios smaller than 1. Average of the recovery for the observed data on the 5 and 6 August 2020. Only overshoot curves with a minimal background amplitude of $R_0 > 10^{10.5}$ are considered. The ratios are chosen in such a way, that, if we observe an overshoot curve like shown in Figure 1, all ratios are smaller than 1.

770 Thus, the histograms are clipped at a maximum ratio of 3. The green line and the corresponding number displays the mean for all ratios smaller than 1.

Average of the relaxation for the observed data on the 11 and 15 August 2018. Only overshoot curves with a minimal background amplitude of $R_0 > 10^{10.5}$ are considered. The ratios are chosen in such a way, that, if we observe an overshoot curve like shown in Figure 1, all ratios are smaller than 1. Thus, the histograms are clipped at a maximum ratio of 3. The green

775 line and the corresponding number displays the mean for all ratios smaller than 1. Average of the relaxation for the observed data on the 5 and 6 August 2020. Only overshoot curves with a minimal background amplitude of $R_0 > 10^{10.5}$ are considered. The ratios are chosen in such a way, that, if we observe an overshoot curve like shown in Figure 1, all ratios are smaller than 1. Thus, the histograms are clipped at a maximum ratio of 3. The green line and the corresponding number displays the mean for all ratios smaller than 1.